David A. Bonneau
PhD Student
Queen's University
36 Union St., Kingston, ON, Canada

September 4th, 2019

To: Dr. Andreas Günther
Editor - NHESS

I would like to submit the revised manuscript entitled "*3-Dimensional Rockfall Shape Back-Analysis: Methods and Implications*" for your review. Major changes have been implemented to the manuscript based upon the comments of the two reviewers. Notable changes include:

- Condensed the introduction based on suggestions from Reviewer 2.
- Moved the section describing the geology of the White Canyon to Section 3.2. This move was done intentionally to highlight that this study is about the methods used not the results of from the study slope.
- Results was re-written to provide clarity, as suggested by all two reviewers.
- Discussion was improved to discuss the merits of each of the methods.
- Figures 6, 9, 10, 11 & 12 and their respective captions were updated following guidance from reviewers to provide additional clarity of the presented results.
- Additional references suggested by Reviewer 2 were included where appropriate.

All changes made to the manuscript were tracked in the attached word document. The logic for each of the changes are outlined on the following the author's responses to the reviewers. A separate word document includes the manuscript with all the changes accepted.

Correspondence regarding the submission should be directed to the following email and telephone number:

David A. Bonneau
Email: david.bonneau@queensu.ca
Tel: +1 (343) 364-3765

Thank you again for your consideration of our paper.

Sincerely,

David A. Bonneau

Response to Reviewer 1

The authors would first like to thank the reviewer for their comments and suggestions.

1. **The authors propose the "Minimum bounding sphere" fitting model (Section 2.2.4). Why the results of the fitting model are not proposed in Figure 13?**

The minimum bounding sphere approach was not included in Figure 13 as it would result in every block plotting at the top of the ternary diagram (see Figure below). In addition, every single block would be classified as cubic. In the minimum bounding sphere approach, all of the calculated dimensions are equal (i.e. A = B = C). However, for completeness, the plot could be included, if required.

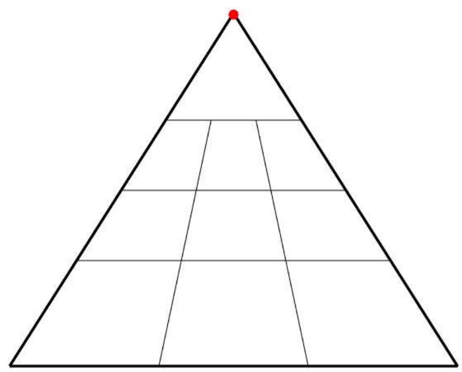

Figure 1 – Sneed and Folk diagram presenting the results of the minimum bounding sphere approach for the 50 rockfall objects.

2. **RFSHAPZ is one of the novel fitting methods. What does "RFSHAPZ" means? Is the method derived from other approaches? Why Fourier series, Gaussian and sum of sines fits? It there a particular reason? Which is the size of the point cloud the authors refer to?**

The name RFSHAPZ is used to reflect rockfall (RF) and the derived shapes (SHAPZ). To the authors' current knowledge, the method is not derived from other approaches. Any curve fitting method can be easily implemented in the code which we have developed. For this study, we chose to implement the Fourier, Gaussian and Sum of Sines approaches, to examine the effect of the variation in curve fitting approach each provides. Both the Sum of Sines and Fourier approaches try to fit a curve to a periodic signal. The main difference is that the Sum of Sines equation includes the phase constant and does not include a constant (intercept) term as in the Fourier approach. The Gaussian approach attempts to fit peaks in the data series. The text can be modified to add further clarification.

The authors are not entirely sure what is meant by "…the size of the point cloud the authors refer to?". All of the synthetic blocks were based on sculpting a 1 m^3 cubic mesh into the shapes presented in the Sneed and Folk diagram.

3. **RFCYLIN is the other novel fitting method. Similarly, what does "RFCYLIN" means?**

The name is to reflect rockfall (RF) and the use of cylinders (CYLIN) in calculating the dimensions of the rockfall objects. The text will be modified to reflect this description.

4. **What differs manual methods 1 and 2?**

Manual 1 and 2 reflects two different people who manually measured the orientation and dimension of the mutually orthogonal dimensions of the dataset of 50 rockfall blocks from the White Canyon. In Line 30 on Page 12, we state that two sets of independent manual measurements were made. The authors will add further clarification to outline what was measured.

5. **The authors should compare the results of automatized methods to the data obtained through a non-automatized method, say, the manual approach which is considered as "true". This will help in defining the best approach.**

The authors are not sure which cases the reviewer is referring to. In the comparison with the synthetic block dataset, all dimensions calculated with each fitting method were compared to manual measurements of each of the blocks. This comparison formed the basis of the error analysis which was conducted.

In the case of the 50 rockfall blocks from the White Canyon, given the variation in the both sets of manual measurements (Figure 13), the authors were hesitant to define one of the measurements as “true” to compare against. This is further illustrated with the example of the single block in Figure 14. Five different independent manual measurements of the dimensions were conducted for the rockfall object. All of the manual measurements indicated that the rockfall object is being classified as very bladed. The adjusted bounding box, least-squares ellipsoid, RFSHAPZ fits and the RFCYLIN approach all resulted in the rockfall object being classified as very elongate. The bounding box classified the rockfall object as either compact-platy to platy. The spherical fit, as always, classified the rockfall object as compact. This is a direct result of the fact that all calculated dimensions are equal when using the spherical fit. This example hopefully illustrates that automated methods should not be blindly used and the method used should consider the expected block shape given the rockmass structure.

The second reviewer addressed that an addition to the discussion on the methods regarding computation and accuracy should be added. The authors will add and provide recommendations on implementing the different methods.

Response to Reviewer 2

The authors would first like to thank the reviewer for their comments and suggestions. The authors would like to point out that there is limited to no work that can be compared to the results of this study. The study was meant to highlight the different methods that can be used to analyze the shape of rockfall events using TLS remote sensing data. This is then demonstrated with application to a case study in the White Canyon, British Columbia, Canada.

In terms of the modelling component, the authors agree with the reviewer. In fact, this is planned future work for another paper. If we must include it here, this will require description of the model, input parameters, parametric analysis and output information, as well as discussions of the study output. This would likely be 6 or more additional pages of text and numerous figures, which will put this well over a reasonable length of paper. We would prefer to keep this work as an additional paper.

Abstract
It would help the reader to estimate the importance of the paper if the novel approaches or so far un-answered
knowledge gaps that the paper suggests to answer are shortly presented in the abstract.

Added in the abstract.

P1 lines 16-17: "a database of close to 5000 rockfalls is presented…" – the authors do not present the database, or
any other database which they refer to (50/60 blocks referred to later in the results). Either present the databases
in supplemental materials or not state implicitly that you present them.

This will be updated in the abstract.

Introduction
General: What is the importance of 3-D block mapping for rockfall hazard assessment?
The Introduction could benefit from more reference to previous studies which discuss that issue, and perhaps to
point out the importance of the 3-D block classification for rockfall hazard estimation worldwide (as opposed to
other simplified block shape methodologies, which were proven to be relatively robust so far). At current stage –
this link is missing and the importance of the study is not well constrained.

P1 line 25: perhaps add a short description of rockfall triggers.

Added.

P2 lines 5-8: there are more large scale works that can be mentioned as previous works on frequency-magnitude
and return periods (e.g. Malamud et al., 2004, Wieczorek and Jäger, 1996).

The suggested publications have been added as references in these lines.

P2 line 28: what do you mean by 'quickly' and 'with substantial detail'? – how quickly? To what extent of detail?

What was meant by "quickly" is that a TLS system is quite portable, is mounted on a tripod and can be deployed as soon as the site is accessed. There is no need to establish a baseline data set as is the case with radar systems, for example. In terms of detail, point clouds captured with TLS systems can have sub-millimeter scale point spacings. These sentences will be altered for clarity and references can be added.

Section 1.1: rockfall shape were previously described in literature and most rockfall hazard programs use some simple geometry shape for falling blocks – providing relatively good results (e.g. Guzzetti et al., 2002). Please address what was previously used for hazard assessment and what is the novelty that TLS 3-D measurements (or the current study) contribute to rockfall hazard? Please provide references to emphasize the importance / augmentation of TLS rockfall shape determination over previous methodologies simplifications.

STONE (Guzzetti et al., 2002) uses a lumped mass approach to simulate the trajectory of rockfall, such that all of the mass is concentrated in a point. Therefore, the size and shape of the rock being simulated are not considered. More recent work, using rigid body physics (e.g. Sala, 2018) can explicitly capture the interactions of the object's geometry and the terrain. These simulations, including the ones of Glover (2015), show that the true 3D shape can have an influence on the runout of the rockfall object. Utilizing TLS, we can capture the exact shape and location of the block detachment location. These cases can then be explicitly incorporated into rockfall simulations for both calibration of the model and development of more representative hazard mapping.

In comparison to previous approaches for rockfall hazard assessment, TLS offers the ability to capture a large section of slope in great detail. Structural kinematic analysis can be completed using the scan data. The work of Lato et al. (2010) demonstrate a workflow to incorporate TLS into rockfall hazard assessment. The TLS scan provides a permanent record of the slope at a given point in time. With multi-temporal data, change detection can provide insight into locations where rockfall activity is impending or has occurred.

It should also be mentioned that in P3 Lines 2 to 4, the authors reference the works of Glover (2015) and Sala (2018) which demonstrate the effects of rockfall shape on the runout distances when using 3D shapes in numerical simulations.

P4 line20: what is the CN main line?

The CN main line is the primary rail track that is situated at the base of the White Canyon. The wording in this sentence has been altered to improve clarity.

Results

In general – there is not a word mentioned on the size of the mapped rockfalls in the results or in the discussion. It will be better to include these – and also power-law size/volume distributions so the readers from other places can relate your database and its applicability to their own study cases and areas.

Work on the frequency-magnitude relationship has been completed by van Veen et al., (2017) using a subset of the database. The focus of this work was on the shape of the rockfall events, not the frequency-magnitude relationships. The monitoring at the White Canyon study site has not been conducted for long enough time period to generate realistic frequency-magnitude relations for larger volume events, and work is ongoing within the research team on this topic

Section 3.2 – what are the size ranges of the rockfalls in the 160 and the 50 blocks selected?

The volumes range from 1 m^3 up to 130 m^3 as the largest event recorded. This information will be added in the results section.

Discussion

In general – the discussion part is relatively short compared to other sections of the manuscript (e.g. Methods or Results). I believe it should be better balanced, as currently the discussion about the insights obtained from the analysis and their implications for other studies were not sufficiently extracted from the data. This could also be achieved by answering the following suggested issues:

Most of the rockfall objects in the study case were classified as 'very bladed' or 'very elongate'. Please consider
discussing the possible source for that – i.e. the local geology and structure of the cliff-face or any other factors.

This is a direct result of the foliation and orientation of the joint sets within the gneiss. As a result, the blocks trend towards the 'very bladed' or 'very elongate' shapes. Details regarding this will be added in the discussion.

About 30% of the identified 'feasible for analysis' rockfalls were included from the suggested methodology (50out of 160) due to irregular morphology (not to mention ~4800 excluded cases of less than 1 m^3). Consider discussing the amount of 'good' identified rockfalls valid for using your suggested methodology and relate to how much you assume it is reliable for application in the real-world.

The greater than 1 m^3 threshold was set based on a criteria in CN's Rockfall Hazard Rating system (RHRA: Abbott et al., 1998) which focuses on the rockfall events that are greater than 1 m^3. This will be clarified in the text.

The reviewer's comment: "amount of 'good' identified rockfalls valid for using your suggested methodology and relate to how much you assume it is reliable for application in the real-world", is not addressed specifically in this paper. This is in part due to the temporal frequency of scanning. It has been shown by a number of authors (e.g. Veen et al. (2017), Williams et al. (2018) and Williams (2017)) that temporal frequency of monitoring has direct implications for the size and shape of the rockfalls that can be detected using remote sensing methods. As longer times elapse between scan intervals, several smaller rockfall events may occur from a location, with the result that the detected shape and volume is larger than would be the case for any of the single events, The proposed methodologies used in this study will work regardless of the input data and will classify the rockfall shapes accordingly. In more real-world situations, where there is potentially even less data available, large rockfall events could be detected which are in reality a series of smaller coalescing rockfall events. This would then have implications for calculated return period but also the shape. Therefore the concept of "good" is not easily quantified. Ongoing work to characterise rockfall shapes, related to slope geometry and rockfall shapes may yield some future logic about "good", and to determine which rockfalls, identified from change detection, should be rejected from analysis as they are likely to be the result of coalescence of several events.

The events smaller than 1 m^3 were excluded based on the RHRA criteria discussed above. In addition, the authors wanted to use a reasonably manageable subset of the data for a preliminary analysis of the rockfall database in order to demonstrate the methods.

P13 lines 20-24 (Results) + P14 lines 25-27 (Discussion): All suggested automatic methods failed to predict the shape of the single exemplary object (very elongated) with relation to its manual measurements (very bladed). Please consider discussing: (1) the significant contribution or advantage for using the automated methods vs the manual measurements; (2) the significant contribution of the two newly suggested methods in the current study over previously used methods.

The exemplary object used for the analysis represents one of the more complicated geometries used in the analysis. This was done purposefully to highlight that in these cases where there is deviation in the shape classification depending on the methods used. The authors have added additional object that is less geometrically complex to demonstrate a case where all the methods align in the shape classification.

Do you consider any scaling factor or effect on your results and conclusions? It appears that most of the discussed rockfalls in the manuscript are of very small size (up to 1-2 cubic meters) compared to other slopes and areas in the world reported in literature (up to tens and even hundreds of cubic meters at places). Please consider discussing the size of the blocks in the database (volume-frequency power laws) and its implications for larger scale blocks and volumes.

This database has been collected between a select period of time and we have seen volumes ranging between 1 and 130 m^3. We have not been monitoring long enough to see the larger volume events.

There are also a number of recent studies that have demonstrated the influences of temporal frequency of monitoring. van Veen et al. (2017), Williams et al. (2018) and Williams (2017) highlight these considerations where depending on the time-frame analyzed, large rockfall events are actually multiple smaller coalescing events.

P14 lines 19-24: Consider discussing the superiority of your suggested methodology (if such exists) – how much computation time / effort do these new models require – versus how better is the accuracy they obtain and how significant it is for more successful rockfall hazard estimation? Which one of them would you recommend for use (at least in your case study – and if you can – try to recommend for other readers).

Considering the definition given by Sneed and Folk (1958) of how to measure shape, the RFCYLIN approach is most closely aligned. The RFCYLIN approach, however, is the most computationally demanding in comparison to the other methods. The RFSHAPZ approach was generated to deal with cases where the surface of the rockfall being analyzed is quite rough and is an attempt at averaging the dimension being calculated.

The bounding box approach should absolutely not be used in any case. All results will be biased towards the cubic end of the Sneed and Folk diagram. If a bounding box type of approach is going to be implemented, it is necessary to implement the adjusted approach. In addition, the adjusted bounding box approach is one of the simpler methods to implement in comparison to the RFCYLIN and RFSHAPZ approaches.

The authors will elaborate more and provide recommendations on implementing the different methods.

Conclusion
Please try to confine the conclusion to insights from the current study only (for example – first paragraph in P15 lines 17-21 cites conclusions from previous studies.)

Theses sentences will be altered to improve clarity.

Please consider actively stating your opinion by suggesting a priority for block shape methodologies: which is most adequate for most cases and which is the less adequate. Try to list them by priority or robustness of success potential to predict real-world rock block shape.

This has been added.

Figures

Figure 2: Please consider a better World location map for readers outside Canada / N America.

Figure 6: Please refer in the figure cation to the relevant studies which presented the different models shown in
the plot.

The appropriate references can be added to the figure caption.

Figure 9: As the main results presented in this study – please consider putting more effort in presenting the data more vividly in this plot. There is a lot of white space and very little data presented.

The decision to present the data in this form was deliberate. It was done purposefully to illustrate spatially the difference in using each of the methods to calculate the dimensions and as a result, the classified shape.

The abbreviations at bottom legend are never referred to in the text or figures. Especially the ones of 'RFSHAPZ_???' should be at least detailed once in the text or figure.
Please add the 'Cubic, Platy, elongated…' the corners of the plots for clarity.

The appropriate abbreviations have been added to the figure caption.

Figures 10-11: the abbreviations at right-hand legend are never referred to in the text or figures.

The descriptions of each of the abbreviations can be included in the figure captions for both Figures 10 and 11.

Added.

Figure 12: please indicate the location of each of the plots (A, B) on Figure 3 of the study area. What are the sizes or size range of the rockfalls indicated here? It is not mentioned in the text or figures. How do these sizes relate to the declared identification threshold detailed in the Methods?

The figure has been updated.

3-Dimensional Rockfall Shape Back-Analysis: Methods and Implications

David A. Bonneau[1], D. Jean Hutchinson[1], Paul-Mark Difrancesco[1], Melanie Coombs[1], Zac Sala[1,2]

[1] Department of Geological Sciences and Geological Engineering - Queen's University, Kingston, Ontario, Canada, K7L 3N6
[2] BGC Engineering Inc., Vancouver, British Columbia, Canada, V6Z 0C8

Correspondence to: David A. Bonneau (david.bonneau@queensu.ca)

Abstract. Rockfall is a complex natural process that can present risks to the effective operation of infrastructure in mountainous terrain. Remote sensing tool and techniques are rapidly becoming the state of practice in the characterization, monitoring and management of these geohazards. The aim of this study is to address the methods and implications of how the dimensions of 3-dimensional rockfall objects, derived from sequential terrestrial laser scans (TLS), are measured. Previous approaches are reviewed, and two ~~novel algorithms~~new methods are introduced in an attempt to standardize the process. The approaches are applied to a set of synthetic rockfall objects generated in the open-source software package Blender. ~~In addition, a database of close to 5000 rockfalls~~Fifty rockfall events ~~is presented~~ derived from sequential TLS monitoring in the White Canyon, British Columbia, Canada are used ~~for~~ to demonstrate the application of the proposed algorithms. This study illustrates that the method used to calculate ~~in which~~ the rockfall~~'s~~ dimensions ~~are calculated~~ has a significant impact on how the shape of a rockfall object is classified. This has implications for rockfall modelling as the block shape is known to influence rockfall runout.

1 Introduction

In steep mountainous regions around the world, infrastructure such as highways and railways may be subject to rockfall hazards. A rockfall can be defined as discrete fragments of rock which have detached from a cliff and subsequently fall, bounce and roll as the fragments move downslope by gravity (Hungr et al., 2014). Rockfalls can triggered by several ~~different~~ factors such as: freeze-thaw cycles, weathering, heavy rainfall, root action, seismicity and others (Volkwein et al., 2011). ~~Rockfalls are also characterized by~~ H~~h~~igh energy and mobility, are also characteristics of rockfalls making them a major cause of landslide fatalities (Guzzetti et al., 2004). Moreover, these geohazards can result in economic losses due to service interruptions and equipment damage.

To assist in the management of these geohazards, a rockfall hazard analysis can be undertaken to qualitatively or quantitatively define the rockfall hazard present along a section of linear infrastructure. A typical rockfall hazard analysis involves the compilation of known rockfall events over a specific spatial scale and within a set period of time (Volkwein et al., 2011). Inventories aim to provide a better understanding about the spatiotemporal occurrence and magnitude of events (Froude and Petley, 2018). Ultimately, temporal trends can be identified from an inventory, which supports a more systematic mapping of hazards in the region to help mitigate future losses. It may also be useful to discern any long-term changes that are projected, as extreme weather events are expected to increase in both frequency and magnitude within a changing climate (Cloutier et al., 2016).

Once an inventory has been assembled, power law distributions have been suggested to characterize the frequency-magnitude relationship for rockfall at the study slope (Hungr et al., 1999). Using the rockfall frequency-magnitude relationship at the study slope, characterized by specific geological and geomorphological features, return periods for select volume ranges can be determined (~~(~~Wieczorek and Jäger, (1996); Hungr et al., (1999); Dussauge et al. (2003); ~~(~~Malamud et al., (2004)).

Remote sensing techniques, such as terrestrial laser scanning (TLS), have been used to characterize and monitor rockfall hazards (Abellán et al., 2014; Jaboyedoff et al., 2012; Telling et al., 2017). Single epoch TLS scans can be used for structural characterization of discontinuity orientations (Lato et al., 2009), the determination of the size and spatial distribution of potentially unstable rock mass volumes (Sturzenegger et al., 2011) and the back-calculation of rockfall volumes based on discontinuity orientations of identified rockfall scars (Santana et al., 2012). Work by ~~(~~Lato et al.~~,~~ (2012), demonstrate how TLS can be integrated into rockfall hazard assessments along road cuts. Rockfall magnitude, block size distribution and block shape distribution were ~~shown to be capable of being~~ measured using surface models derived from TLS scans. This information can be directly integrated into rockfall modelling for rockfall hazard evaluation.

With multi-temporal TLS datasets, c~~C~~hange detection algorithms, such as M3C2 (Lague et al., 2013), as an example, can be used to identify areas of loss on slopes (i.e. rockfall) between sequential TLS scans. The location, volume and dimensions of rockfall on the slope can be calculated and populated into a database, as demonstrated by Rosser et al. (2007), Guerin et al. (2014), Tonini and Abellan (2014), van Veen et al. (2017), Janeras et al. (2017) and Williams et al. (2018). In several of these studies, smaller magnitude rockfalls have been identified, which are ~~often~~ generally not observed during field inspections performed from the base of the slope. Furthermore, smaller rockfall events have been shown to bound the area of ~~a~~ larger deforming portions of the slope (Kromer et al., (2015)).

Recent work by Williams et al. (2018) make use a fully automated terrestrial laser scanning system to near-continuously monitor a section of coastal cliff in the United Kingdom. With near real-time processing capabilities, they demonstrate the influence of temporal acquisition rate on the calculated frequency-magnitude relationship for rockfall at the study slope. They demonstrate that more frequent monitoring captures a higher proportion of smaller magnitude rockfall events, which represents a higher frequency magnitude scaling coefficient. However, due to the 2.5D nature of the volumetric analysis, smaller magnitude events resulted in a higher degree of volumetric uncertainty, due to edge effects compounded when 3D change maps are converted to 2.5D raster datasets.

Rockfall pre-failure deformation can also be detected and quantified using TLS systems (Abellán et al. 2010, Royán et al. 2014, Kromer et al. 2015a, 2015b). Deformation signatures prior to rockfall events can be associated with entries in rockfall databases to assist with management of rockfall hazards at a given slope (Kromer et al., 2017b; Rowe et al., 2017).

With the rapid automation of TLS acquisition and change detection processing workflows (Kromer et al., 2017; Williams et al., 2018), we practitioners are able to evaluate potential rockfall events and their characteristics quickly and with substantial detail (Abellán et al., 2014). TLS systems are portable and can be deployed on a tripod as soon as the site is accessed. There is no need to establish a baseline dataset as is the case with radar systems, for example (Teza et al., 2008). In addition, TLS systems can achieve high spatial resolution of measurements (Pesci et al., 2011). These strengths of TLS systems facilitate detailed back analysis of rockfall events to assess characteristics which can then be used One of the key characteristics of the data collected is the rockfall shape and dimensions for ongoing rockfall hazard analysis. With the recent advances in rockfall modelling with rigid body physics, models can utilize the exact shape and location position of the block detachment location (Harrap et al., 2019, Submitted). These cases can be used for both calibration of the model and development of more representative hazard mapping. Preliminary studies of the rockfall runout with respect to rockfall shape have been conducted (e.g. by Glover, (2015) and ; Sala (, 2018). In their respective works, they Both authors found highlight that the shape of the rockfall object has a pronounced effect on runout behaviour. This behavouir has direct implications for rockfall hazard zoning. Therefore, the ability to characterize the shape of rockfall events is a key component which needs to be considered in generating rockfall databases from sequentiail TLS scans. A variety of different formulations have been proposed to measure the shape of rockfalls from point cloud datasets, which record the before and after failure geometry. We The authors highlight several methods which have been used in other studies and present two new methodologies to determine the dimensions of a rockfall object.

1.1 Rockfall Shape and Dimensions

The quantification of the shape of a rockfall scar can provide insight into the kinematics of failure and potential runout of detached material fragments. The use of remote sensing techniques and 3D change detection algorithms permits extraction of true rockfall shape, yet limited work has been completed to quantify shape, despite its pronounced effect on runout behaviour (Glover, 2015; Sala, 2018). Shape, as noted by Blott and Pye (2008), is a function of four primary characteristics which include: form, roughness, irregularity and sphericity. Readers are referred to Blott and Pye (2008) for further details on these characteristics.

In 1958, Sneed and Folk introduced a ternary diagram (Fig. 1A) to describe the shape of pebbles based on relations between the long (A), intermediate (B) and short orthogonal axes (C). The three ratios are listed below:

$$\frac{C}{A} \quad (1)$$

$$\frac{A-B}{A-C} \quad (2)$$

$$\frac{B}{A} \quad (3)$$

Based on the three relations described above, particles can be classified into ten different shape classes. The end members of the ternary diagram are: compact (cubic), platy (tabular), and elongated (rod shaped).

The Sneed and Folk ternary diagram has been used in rockfall studies to characterize rockfall dimensions (Benjamin, 2018; van Veen et al., 2017; Williams, 2017). In the aforementioned studies, ~~the method to calculate the dimension of~~ the rockfall dimensions are ~~is~~ based on a bounding box approach. A bounding box defines the minimum extents of a box which fully encloses the set of points defining the object. In this study, the bounding box is oriented such that the edges of the calculated box are parallel to Cartesian coordinate axes.

Currently there is no standardized method to determine the dimensions of a rockfall object. There is uncertainty in evaluating both the distance and orientation of the axis lengths. This is compounded by the fact that there is ambiguity ~~if~~ about whether the axis measurements are to be mutually orthogonal or not. In this work, we address these uncertainties and propose standardized methods to evaluate the dimensions of a rockfall object.

1.2 Objectives

In this work, we address the process of extracting information regarding rockfall dimensions from remotely sensed datasets. The primary objectives of this work are summarized below:

1. Review current approaches used to determine the dimensions of 3D rockfall objects.
2. Present two ~~novel~~ new approaches for extracting the dimensions from 3D rockfall objects represented by point clouds.
3. Apply all of the approaches to a dataset of synthetic 3D rockfall objects.
4. Implement the proposed approaches on a rockfall database derived from terrestrial laser scanning (TLS) at the White Canyon in the Thompson River Valley in Interior British Columbia, Canada.

5. Determine which method(s) provide the most accurate measurements of the objects’ three mutually orthogonal principal axes.

A rockfall object in this context is defined as: a 3-dimensional (3D) point cloud or mesh that approximates the geometry and volume of rock that detached from the slope.

~~1.3 Study Slope – The White Canyon, British Columbia, Canada~~

~~The White Canyon (50.266261°, -121.538943°), located in the Thompson Rail Corridor in Interior British Columbia, Canada, is an operationally challenging rock slope (Fig. 2). Rockfall and the movement of debris originating from the steep slopes present geohazards to the safe operation of the Canadian National (CN) main line, which runs at the base of the slope adjacent to the Thompson River (Bonneau and Hutchinson, 2017; Kromer et al., 2015b; van Veen et al., 2017).~~

~~The morphology of the White Canyon is highly complex; differential erosion has formed a morphology which varies across the Canyon and consists of vertical spires and deeply incised channels. The active portion of the Canyon reaches up to 500 m in height above the railway track. The Canyon spans approximately 2.2 km between Mile 093.1 and 094.6 of the CN Ashcroft subdivision. A series of short portals (tunnels) mark the entrances to the Canyon; a portal can be found on either side of the Canyon. A third portal~~ short tunnel ~~is located in the middle of the Canyon through a ridge which separates the eastern and western portions of the site.~~

~~Two dominant geological units comprise the geology of the White Canyon. The primary unit is the Lytton Gneiss. The Lytton Gneiss is a quartzofeldspathic gneiss with amphibolite bands, containing massive quartzite, amphibolite and gabbroic intrusions (Monger, 1985). In the most western extent of the Canyon, towards the west tunnel portal is the other dominant unit, the Mt. Lytton Batholith. The Mt. Lytton Batholith is a distinctly red stained unit which is composed of granodiorite with local diorite and gabbro. The red staining of the rockmass, is thought to be a direct result of fluids originating from the weathering of hematite in overlying mid-Cretaceous continental clastic rocks. Two sets of dykes have intruded the Lytton Gneiss, within the White Canyon. The first dyke set consists of tonalitic intrusions which are believed to be related to the emplacement of the Mt. Lytton Batholith (Brown, 1981). The second dyke set is a series of dioritic intrusions which cross cut the Lytton Gneiss and tonalitic dykes. These dioritic intrusions are believed to be part of the Kingsvalle Andesites (Brown, 1981).~~

2 Methodology

~~As noted above, t~~The methodology involves applying a variety of approaches ~~for~~ to measure the ~~ing~~ geometry of ~~the~~ irregularly shaped blocks ~~to~~ and evaluating the output using the ~~a synthetic dataset generated to represent the~~ range of shapes described in the Sneed and Folk ternary diagram (Section 2.1). Both synthetically generated (Section 2.1) and real rock shapes were assessed. The methods by which data was collected and processed, for the real rock shapes using both terrestrial laser scanning (TLS) and Structure-from-Motion Multi-View-Stereo (SfM-MVS) photogrammetry are discussed in Section 2.2. Section 2.3 presents the methodology used to extract rockfall information from 3D change detection. Section 2.4 describes the six approaches used to extract dimension information from 3D point clouds of rockfall shapes.

2.1 Synthetic Block Dataset

A synthetic block dataset was generated in the open-source software package Blender (Blender, 2018) using the process described by ~~.~~ Sala (2018) ~~outlines the process used~~ to generate synthetic blocks for rockfall simulation. In general, the process involves the sculpting of cubic meshes that encompass 1 m^3 of volume~~cubic meshes~~. Mesh sculpting in Blender allows for the displacement of mesh geometries into a variety of different shapes, taking into consideration block form characteristics, such as angularity. Once a shape has been created, its mesh is ~~subsampled~~subdivided, increasing the number of vertices on the shape's surface to better match the point density which ~~could~~ can be achieved from the TLS data described in the following sections. The mesh vertices are then exported, creating a synthetic rockfall block point cloud. Blocks corresponding to each major class in the Sneed & Folk ternary diagram were created. For each class, (i.e. platy, elongate, cubic, etc.) a rounded and an angular version, as defined by Powers (1953), of the block was generated. Fig. 1B &1C displays examples of the blocks used in this study.

2.2 Remote Sensing Data Acquisition

The following subsections (2~~3~~.2.1 & 2~~3~~.2.2) outline the remote sensing techniques that are used in this study to collect point cloud data to define the geometry of real rockfalls. ~~.~~

2.2.1 Terrestrial Laser Scanning (TLS)

Terrestrial laser scans were taken with an Optech Ilris 3D-ER terrestrial laser scanner (Fig. 1D). The Optech Ilris has a manufacturer-specified accuracy of 7 mm in range ~~from a distance 100 m~~ and 8 mm in vertical and horizontal directions for data collected from a distance of 100 m (Optech, 2014). The maximum range for the Optech Ilris is approximately 800m with 20% target reflectivity (Pesci et al., 2011).

Due to the complex geometry of the ~~ical nature of the~~ rock slopes in the White Canyon, several overlapping scans from different vantage points were captured to minimize occlusions and to decrease the lateral incidence angle in the scans of the slope. Point spacing for each scan varied between 7 to 10 cm. The scan site locations are displayed in Fig. 3, along with a timeline of the scans used in the study. Scans were taken approximately every 2-3 months starting in November 2014. The last set of TLS scans used in the analysis were taken in December 2017.

To process the TLS scans, the scans were first parsed using Optech Parsing software. Once parsed, vegetation, mesh, and railway infrastructure components such as slide detector fences, were manually removed from the raw point cloud using PolyWorks PIFEdit. After the point clouds were cleaned, they were aligned using PolyWorks ImAlign to a common baseline (November 2014). The alignment process consisted of a coarse alignment using point picking and then a fine alignment using an iterative closest point (ICP) algorithm (Besl and McKay, 1992). Areas of known change on the slope were excluded from the alignment process to help improve the alignment between sequential scans (Lato et al., 2015).

2.2.1 Structure-from-Motion Multi-View-Stereo (SfM-MVS) Photogrammetry

Structure-from-Motion Multi-View-Stereo (SfM-MVS) photogrammetry models were generated of both the White Canyon Eastern (WCE) and White Canyon Western (WCW) portions of the White Canyon (Fig. 4). The Agisoft Photoscan Professional V1.3.2 software package (Agisoft LLC, 2018) was used to create the models. The models were generated following a typical SfM-MVS photogrammetry processing workflow (Smith et al., 2016; Westoby et al., 2012).

A Nikon D750 DLSR camera with a Nikkor 50mm f/1.8 prime lens was used for all image acquisitions. An external global positioning system (GPS) was attached to the camera to geotag each photograph. The 282 images used to generate the White Canyon West (WCW) model were captured on 2018-01-30. The 452 images used to generate the White Canyon East (WCE) model were captured on 2018-04-07. 282 photographs were used to generate the WCW model while 452 photographs were used to generate the WCE model. Images were captured with approximately 50 to 60% overlap.

Each of the SfM-MVS photogrammetry models were remotely mapped in PhotoScan to delineate generate masks of the boundaries of bedrock outcrops and channels to create masks in PhotoScan (Fig. 4C). This process is described in detail by (Jolivet et al., (2015). The photogrammetry models and masks were exported and aligned to the TLS datasets in CloudCompare for further analysis. The masks are used in the semi-automated rockfall extraction process that is described below.

2.3 Rockfall Extraction Process

In this study, a similar process as utilized by Tonini and Abellan (2014), Carrea et al. (2015), Janeras et al. (2017), and van Veen et al. (2017) to semi-automatically identify rockfall locations and extract information related to the dimensions of each rockfall event is implemented. A generalized rockfall extraction process is illustrated in the flow chart in Fig. 5.

The process can be summarized as follows: once the TLS scans are cleaned and aligned, the process involves computing the change between sequential scans taken at times *A* and *B*. Distances are computed from *A* to *B* and then *B* to *A*. This process determines the front and back of each rockfall event in each respective scan. A minimum change threshold is then applied, this threshold is typically based on the calculated limit of detection. The point clouds of the fronts and backs of all rockfall events are then merged to generate rockfall objects. Variants of DBSCAN (Ester et al., 1996) are then implemented to cluster individual rockfall events which have occurred between time *A* and *B*. The dimensions, volume and other parameters of each individual rockfall event can be calculated and then populated into a database for further analysis.

In this study, to compute the change between sequential TLS point clouds, the process ~~-~~outlined ~~in~~ by Kromer et al. (2015a) is utilized. The distance calculation is very similar to M3C2 (Lague et al., 2013), where distances are calculated along normal vectors defined by slope geometry within a specified radius from the point. The change is then filtered based on the limit of detection. The limit of detection (LOD) can be defined based on the registration error (Abellán et al., 2014). In this study, we take two times the standard deviation (95% confidence interval) of the registration error to define the limit of detection. The LOD equates to approximately 5 cm in the summer months and 7 to 10 cm in the winter months (i.e. October to February). The higher limit of detection in the winter months corresponds to a higher standard deviation in the registration error (alignment). ~~The h~~Higher standard deviations correspond~~s~~ to the winter scans, where there is ~~a higher amount of~~ generally more humidity in the air and possibly water on the slope surface, which have ~~all~~ been ~~noted~~ found to influence the alignment process (Abellán et al. 2014).

Detectable change was then filtered based on the LOD, to resolve clusters of points that represent the scars (backs) of rockfall events. This process was repeated, conducting the change detection in the opposite direction to resolve the fronts of the rockfall objects. DBSCAN (Ester et al., 1996) was then used to cluster areas of change. The same parameters as van Veen et al. (2017) are used for the DBSCAN clustering (i.e. search radius of 30 cm and a minimum of 12 points to define a cluster).

To resolve rockfall events as opposed to debris movements, we utilized the masks mapped on the SfM-MVS photogrammetry models. ~~As opposed to van Veen et al. (2017), who implemented a 2.5D mask, a true 3D mask is used to avoid misclassification.~~ The geometric centroids of each cluster are used to search and find the 10 nearest neighbours within the mask point cloud. Based on the classification of the 10 nearest neighbours within the mask point cloud, a vote is conducted to classify the centroid as either a debris movement or rockfall depending on the mask classification (i.e. bedrock vs. channel).

2.4 Model Fitting

The following subsections present the background for each of the models used to determine the dimensions of the rockfall objects. Each of the approaches were implemented in MATLAB (Mathworks, 2018).

2.4.1 Bounding Box

A bounding box or enclosing box defines the minimum extents of a box within which all points are contained. In this study, the bounding box is oriented with the edges of the calculated box parallel to the Cartesian coordinate axes (Fig. 6A).

2.4.2 Adjusted Bounding Box

The adjusted bounding box approach differs from the bounding box approach in that the orientation of the box is not subjected to any constraints. In this study, singular value decomposition (SVD) (Golub and Loan, 1996) is used to determine the orientation of the object relative to the principal axes in Cartesian space. SVD is used because this process can handle any $m \times n$ matrix whereas eigenvalue decomposition can only be applied to certain classes of square matrices (Golub and Loan, 1996). The direction of most variance using SVD is determined and the point cloud is rotated to align with the direction of maximum variance with the x-axis in Cartesian space. This results in the x-axis of the box being aligned with the longest dimension of the object. A bounding box can then be calculated for the point cloud (Fig. 6B).

2.4.3 Least-Squares Ellipsoid

An ellipsoid can be defined as a closed quadric surface that is the analogue of an ellipse. To fit an ellipsoid to the point cloud defining a rockfall object, an algebraic form linear least-squares ellipsoid fit (Schneider and Eberly, 2003) is implemented. An algebraic fitting model was selected as opposed to an orthogonal fitting ellipsoid to reduce computing time and to benefit from the advantages of solving linear least-squares problems (Li and Griffiths, 2004). The algorithm generates a least-squares ellipsoid fit of the input point cloud (Fig. 6C). Further details on the algorithm and derivation can be found in Schneider and Eberly (2003).

2.4.4 Minimum Bounding Sphere

To fit a minimum bounding sphere to the point cloud, Welzl's 1991 algorithm is implemented. The algorithm computes the smallest sphere enclosing a set of points in 3-space in linear time (Fig. 6D). For further details on the algorithm, readers are referred to Welzl (1991).

2.4.5 RFSHAPZ

In this study, the RFSHAPZ (Rockfall Shape) approach is introduced. The approach can be broken into four main steps: (1) Point cloud preparation, (2) Voxelation, (3) Distance calculations, and (4) Curve fitting. Figure 7 outlines a flowchart for the process used to determine the dimensions of each rockfall object.

Point cloud preparation involves translating each rockfall object so that the object's geometric centroid is centered at the origin of a locally defined Cartesian coordinate system. Once the object is centered at the origin, SVD is used to rotate the object so that the longest dimension is parallel with the x-axis in Cartesian space.

The next step involves generating a voxel grid of the point cloud. A voxel is a 3D volume element that represents a numerical value. For this study, the default voxel cube size is defined as a function of the point spacing. We calculate the average point spacing of the surfaces that make up the rockfall object, and then double the value to determine the voxel size. The size of the voxel is therefore a function of the point spacing and can be adjusted depending on the rockfall object. The voxel grid is used to provide a spatial context for the rockfall object and allows all points within each voxel to be stored for further analysis. Once the voxel grid is established, for each voxel grid line in the XY and XZ planes, we calculate the maximum Euclidean distance between points within populated voxels (Fig. 6E). The calculated distances are plotted along each grid line. Curves are then fit to each of the distributions, utilizing a Fourier Series fit, a Gaussian fit and a Sum of Sines fit. An overview of each of the fitting methods is provided below.

The Fourier series is a sum of sine and cosine functions that describes a periodic signal. In this study, we use the trigonometric form of the series which can be expressed as:

$$y = a_0 + \sum_{i=1}^{n} a_i \cos(iwx) + b_i \sin(iwx) \tag{4}$$

where a_0 is a constant term and is associated with the $i = 0$ in the cosine term. w represents the fundamental frequency of the signal, and n is the number of terms in the series. For this study, n is fixed at a constant value of one.

The Gaussian model fits peaks in a data series, and is given by:

$$y = \sum_{i=1}^{n} a_i e^{\left[-\left(\frac{x-b_i}{c_i}\right)^2\right]} \tag{5}$$

where a is the amplitude, b is the centroid (location), c is related to the peak width, n is the number of peaks to fit. For this study, n is fixed at a value of one.

The last curve fitting function used is the sum of sines model. This model fits periodic functions, and is given by:

$$y = \sum_{i=1}^{n} a_i \sin(b_i x + c_i) \tag{6}$$

where *a* is the amplitude, *b* is the frequency, and *c* is the phase constant for each sine wave term. n defines the number of terms in the series. This equation is closely related to the Fourier series described in Section 2.4.5.1. The main difference is that the sum of sines equation includes the phase constant and does not include a constant (intercept) term. For this study, *n* is fixed at a value of one.

2.4.6 RFCYLIN

The last approach introduced and implemented in this study, RFCYLIN (Rockfall Cylinders), draws inspiration from the M3C2 methodology (Lague et al., 2013). The point cloud preparation is the same as was described for the RFSHAPZ approach discussed in Section 2.4.5.

For all points in the cloud defining the rockfall object, we calculate the vector and Euclidean distance from each point to the geometric centroid. The vector is oriented towards the calculated centroid. A cylinder is then projected from each point through the geometric centroid of the rockfall object. The length of the cylinder is set to be greater than the distance calculated between each point and the geometric centroid. After the cylinder has been projected, points are found to be within the cylinder. These points are projected on the vector line and the maximum distance between all points through the centroid is determined. This process results in determining the maximum (longest) dimension of the rockfall object.

Once the maximum distance and vector orientation has been calculated, orthogonal vectors to the vector of maximum distance are then calculated through SVD. To do this step, a plane is projected perpendicular to the vector defining the maximum dimension. Points defining the rockfall object are projected onto the plane. SVD is then used to determine the direction of maximum and minimum variance. These define the vector orientations of the other axes. Once the ~~vector~~ orientations of the orthogonal vectors have been determined, cylinders are projected along each vector to find points which lie within the cylinder. If no points are found to be within the cylinder, we incrementally increase the diameter of the cylinder until points are found to be within the cylinder. These points are then projected onto the vector line defining the centerline of the cylinder. The distance between points along each of the orthogonal vectors are calculated and define the intermediate and shortest dimensions of the rockfall object (Fig. 6F). A flowchart outlining this algorithm is displayed in Fig. 8.

3 Results

The calculated dimensions of the rockfall objects, using each of the techniques described in Section 2, are tabulated for analysis. Section 3.1 presents the results from the analysis of the synthetic block dataset. Section 3.2 presents the results of the analysis on the rockfall objects extracted from the TLS monitoring in the White Canyon.

3.1 Synthetic Block Dataset

The dimensions of the twenty synthetic blocks described in Section 2.1 were measured using the six methods outlined in Section 2.4. In addition, Two independent sets of measurements were made manually by two different members of the research team, to provide a baseline.

The calculated dimensions were plotted on Sneed & Folk ternary diagrams in order to examine the geometric results, as shown in Fig. 9. The data for the smooth (rounded) and angular synthetic objects is are shown on separate diagrams to highlight differences in the distribution of these datasets. Evaluation of the data shows that the calculated measurements for some shapes aligns well, independent of the method applied. The observations made of these data sets include:

- The angular synthetic block dataset displayed the largest spread in the geometry represented by the calculated dimensions, when compared to the smooth rockfall objects.
- The measured dimensions of the very-bladed and very-elongate blocks, at the bottom left and right corners of the ternary diagram respectively, were closely aligned for all methods and manual measurements.
- The angular compact series (i.e. compact-platy, compact-bladed and compact-elongate), showed the greatest divergence between the manual measurements and the automated methods. A number of the methods, including the manual measurements, classified the angular compact-platy block as platy. The methods which did correctly categorize this shape, include the bounding box, the adjusted bounding box, the RFSHAPZ – Gaussian fit and the manual measurements. These measurements, however, are not closely aligned, and display significant spread between the data points.
- With increasing compactness of the synthetic shape, there are challenges with assessing what is the shortest axis with manual measurements. This effect is compounded with increasing angularity of the rockfall object.
- For the angular compact-elongate block, the two manual measurements incorrectly classify the block as compact bladed while all of the calculated dimensions classify the block as compact-elongate.

The results of the rounded synthetic block dataset displayed significantly less spread in the calculated and measured block dimensions relative to the than their angular counterparts. Only the rounded compact-elongate block had classification issues based on the measured or calculated dimensions. The RFCYLIN approach, RFSHAPZ and adjusted bounding box all classified the block as compact-bladed.

In order to analyze the results, the manual measurements were selected as a basis of comparison, with the synthetic blocks. Taking the manual measurements as the best representation of the dimensions of each of the synthetic blocks, the error in each dimension measurement from each of the calculated methods (i.e. A, B & C) could be quantified. Figure 10 displays the results for the rounded synthetic blocks and Fig. 11 presents the results for the angular set. The bounding box and adjusted bounding box approaches were excluded from this analysis since they are a component of the process of how the synthetic blocks were generated within Blender (Sala, 2018).

Overall, the errors associated with the angular dataset are an order of magnitude higher than the rounded dataset (A-axis). In addition, for the A-axis measurements, none of the calculated fits underestimated the dimension, for both the angular and rounded datasets. Relative to the rest of the shapes, the platy series (i.e. compact-platy, platy, very-platy), showed the highest deviations from the manual measurement. Within the angular data series, errors on the order of 20 cm (~20%) were reported for the A-axis measurement.

3.2 White Canyon Rockfall Dataset

The White Canyon (50.266261°, -121.538943°), located in the Thompson Rail Corridor in Interior British Columbia, Canada, is an operationally challenging rock slope (Fig. 2). Rockfall and the movement of debris originating from the steep slopes present hazards to the safe operation of the Canadian National (CN) rail line, which runs at the base of the slope adjacent to the Thompson River (Bonneau and Hutchinson, 2017; Kromer et al., 2015b; van Veen et al., 2017).

The morphology of the White Canyon is highly complex; differential erosion has formed a morphology which varies across the Canyon and consists of vertical spires and deeply incised channels. The active portion of the Canyon reaches up to 500 m in height above the railway track. The Canyon spans approximately 2.2 km between Mile 093.1 and 094.6 of the CN Ashcroft subdivision. A series of short tunnels mark the entrances to the Canyon; a portal can be found on either side of the Canyon. A third short tunnel is located in the middle of the Canyon through a ridge which separates the eastern and western portions of the site.

Two dominant geological units comprise the geology of the White Canyon. The primary unit is the Lytton Gneiss. The Lytton Gneiss is a quartzofeldspathic gneiss with amphibolite bands, containing massive quartzite, amphibolite and gabbroic intrusions (Monger, 1985). In the most western extent of the Canyon, towards the west tunnel portal is the other dominant unit, the Mt. Lytton Batholith. The Mt. Lytton Batholith is a distinctly red stained unit which is composed of granodiorite with local diorite and gabbro. The red staining of the rockmass, is thought to be a direct result of fluids originating from the weathering of hematite in overlying mid-Cretaceous continental clastic rocks. Two sets of dykes have intruded the Lytton Gneiss, within the White Canyon. The first dyke set consists of tonalitic intrusions which are believed to be related to the emplacement of the Mt. Lytton Batholith (Brown, 1981). The second dyke set is a series of dioritic intrusions which cross cut the Lytton Gneiss and tonalitic dykes. These dioritic intrusions are believed to be part of the Kingsvalle Andesites (Brown, 1981).

Analysis of the TLS data collected at the White Canyon study slope between November 2014 and December 2017, using the semi-automated rockfall extraction process resulted in a database of 4960 rockfall events: ~~.~~ 2566 events ~~were identified on the~~ in WCW ~~slopes during the monitoring period, while~~ and 2394 events ~~were documented~~ in WCE. The centroid of each of the detected rockfalls is displayed in Fig. 12. The data plotted in this figure displays that the spatial distribution of rockfall is quite varied across the entire canyon. Rockfalls were documented to occur in all lithologies present in the slope.

A sub-set of ~~50~~ rockfall events were identified and selected from the overall database for further analysis. The volumes of the selected ~~se~~ rockfalls ranged from 1 m^3 up to 130 m^3 which was ~~as~~ the largest event recorded during this period. ~~22 of the rockfall events occurred in WCW while 28 of the events occurred in WCE.~~ As a first pass, only events larger than 1 m^3 were selected from the full database. This selection was based on a criterion in CN's Rockfall Hazard Rating system (RHRA: Abbott et al., 1998) which focuses on the rockfall events that are greater than 1 m^3. ~~-~~The resulting 160 rockfall events were considered large enough that a reasonable estimate of their shape could be made from the point cloud where the data points are spaced at approximately 7 cm apart. ~~The volumes of these rockfalls ranged from 1 m^3 up to 130 m^3 as the largest event recorded.~~ 110 rockfall events were removed from the sub-set due to their ~~complex, multi-lobed~~ shapes. ~~The remaining 50 events were interpreted to be the result of discrete individual events, based on fairly well constrained shape, relative to rockmass structure present at the rockfall source location.~~ It is probable that numerous smaller failures have occurred from that same location (van Veen et al., 2017; Williams et al., 2018) during the three to four months elapsed time between scanning campaigns. ~~.~~ The change detection, ~~however~~therefore, will generate the geometry of an apparent single rockfall which is in fact likely to be the result of several coalesced smaller events, resulting in complex, multi-lobed shapes. ~~Rockfall objects in the database with very complex, multi-lobed morphology were rejected from the sub-set utilized in this analysis.~~ Certainly, the authors~~we~~ cannot be sure about the number of events that might have contributed to the final rockfall object, unless ~~we have~~ without much more frequent scanning intervals. The remaining 50 events were large enough to be of potential impact on the railway infrastructure and were interpreted to be the result of discrete individual events, based on fairly well constrained shape, relative to rockmass structure present at the rockfall source location. Using the six methods outlined in Section 2.4, the dimensions of the 50 blocks were measured. In addition to the automated measurements, two sets of independent manual measurements were also made.

Figure 13 displays the Sneed & Folk ternary diagram for each model fit applied to the 50 rockfall cases in the White Canyon. The bounding box approach resulted in a distribution on the Sneed & Folk ternary diagram that is quite scattered, however, the overall trend is towards a more cubic shape for all of the measured rockfall objects. All possible shapes in the Sneed & Folk classification (i.e. compact, very-elongate) are represented by rockfall object shapes assessed using this method.

The results of the other fitting methods and the manual measurements are in stark contrast to the results of the bounding box approach. None of the other fitting methods nor manual measurements classify any of the 50 rockfall events as cubic or in the compact series (i.e. compact-platy, etc.). All the other fitting methods and manual measurements trend towards very-bladed to very-elongate shape classifications, and are distributed across the lower portion of the diagram.

~~A single~~Two rockfall events were~~as~~ isolated from the 50 events to illustrate the complexities inherent in working with real rockfall shapes, as well as the variations in the calculated dimensions (Sneed & Folk shape classification) using each of the methods implemented in the study (Fig. 14). One of the rockfall objects is more geometrically complex than the other. There is a notch in the upper portion of the more complex rockfall. For the geometrically complex object, ~~Aall~~ the results of the ~~fits used to assess the dimensions of this~~ rockfall event dimension measurements are ~~visually~~ displayed in Fig. 6. The rockfall occurred in the western portion of the White Canyon between June 2015 and August 2015. The rockfall fell from a height 0f approximately 20 m above track level and a number of impact points along the rockfall trajectory were documented from the change detection analysis. The volume of the rockfall event was estimated to be approximately 1.7 m^3, and the shape, although complex, is considered to be well enough constrained that this could be the result of a single event that occurred during that three month period between scans. The other rockfall event analyzed (Fig. 14b) occurred in the eastern portion of the White Canyon between October 2015 and February 2016. This 1 m^3 rockfall occurred above a debris channel in the quartzofeldspathic gneiss host unit. Based on the orientation and spacing of the discontinuities in the surrounding rockmass, it is thought that this event is ~~considered constrained that it could be~~ likely the result of a single event that occurred between the scan dates.

Five different independent manual measurements of the dimensions were conducted for both ~~the~~ of these rockfall objects. For the first object (Fig. 14a), a~~A~~ll of the manual measurements indicated that the rockfall object is ~~being~~ classified as very bladed. The adjusted bounding box, least-squares ellipsoid, RFSHAPZ fits and the RFCYLIN approach all resulted in the rockfall object being classified as very elongate. The bounding box classified the rockfall object as either compact-platy to platy. The spherical fit, as always, classified the rockfall object as compact. This is a direct result of the fact that all calculated dimensions are equal when using the spherical fit.

In comparison, the less complex object was classified as very elongate with all manual measurements and the adjusted bounding box, least-squares ellipsoid, RFSHAPZ fits and the RFCYLIN approach. The bounding box approach resulted in the object being classified as compact-bladed and the spherical fit classified the rockfall object as compact.

In general, when comparing the shape classifications of the dataset of the 50 rockfall objects to the manual shape classifications there were~~was~~ significant differences. When the automated shape classifications were compared to the Manual 1 and Manual 2 shape classifications, the bounding boxing agreed with ~~the~~ Manual 1 and Manual 2 ~~shape classification~~ in 3 of the 50 cases. The adjusted bounding box, ellipsoid fit, each of the RFSHAPZ fits (Fourier, Gaussian and Sum of Sines) and RFCYLIN agreed with the Manual 1 / 2 shape classifications in 29/25, 2/295, 29/30, 29/29, 28/30 and 24/29 of the cases, respectively. In comparison to Manual 2 shape classifications, similarly, in only 3 of the 50 cases, the bounding box agreed with the Manual 2 shape classification. The adjusted bounding box, ellipsoid fit, each of the RFSHAPZ fits (Fourier, Gaussian and Sum of Sines) and RFCYLIN agreed with the Manual 2 shape classifications in 25, 29, 30, 29, 30 and 29 of the cases respectively.

Interestingly, there were only 34 cases where the shape classifications of the two manual measurements agreed with one another. Furthermore, there were only 8 cases of the 50 analyzed where the both manual mappings measurements matched all of the automated approaches, excluding the bounding box and spherical fits. Neither of the two manual classification datasets aligned with any of the spherical fits.

4 Discussion

The shape or form of an object can be classified by assessing aspect ratios of major axes. However, it has been noted that a problem with this approach is that there is no standardised method used to determine axis length or if the axis measurements should be orthogonal or not. Additionally, there is an inherent ambiguity in selecting the geometric axes of a particle (Blott and Pye, 2008). The ambiguity arises with increasing compactness of particles, where all axes lengths are almost equal. In these situations, it is very difficult as well as subjective as to how these dimensions are measured since it is difficult to manually define an orthogonal frame. In this study, the authors have presented and compared six different methods for assessing a rockfall object's dimensions and resulting shape. All of the algorithms have been presented allowing these approaches to be replicated for future works. In addition, the authors have created a synthetic dataset of rockfall objects that can be used to assess new algorithms aimed at determining a rockfall object's dimensions. This synthetic dataset represents a step forward in standardizing methodologies for best-practice in generating remotely sensed rockfall inventories.

The results of this study confirm that the method in which dimensions are measured results in significantly different shape classifications. The authors have demonstrated that a bounding box approach (e.g. van Veen et al., (2017); Benjamin (2018)) can potentially bias the dimension measurements toward a more cubic form, if the orientation of the longest axis of the rockfall object is not parallel with one of the major Cartesian axes. If opting for a bounding box approach to determine the object's dimensions, the adjusted approach should be used instead.

A minimum bounding sphere was shown to be highly inappropriate for dimension extraction in the cases analyzed in this work. The approach results in all dimensions of the object being equal and every single object being classified as compact or equant (i.e. A=B=C). This may be valid for rockfall objects in some narrowly defined geological settings where equant blocks are released by the slope rockmass. In additionFor example, further work is required to assess the applicability of the minimum bounding sphere approach to ~~assess~~ determine the dimensions of detached and rounded cobbles and boulders from select horizons of postglacial river terraces (Bonneau and Hutchinson, 2018a, 2018b).

In comparison to the other methods, the RFCYLIN approach introduced in the study is the most computationally demanding algorithm. The method tries to standardize an approach to measure dimensions, where each axis is measured orthogonally to one another after the longest dimension has been defined. However, occlusions and edge-effects in change detection analysis can result in inaccurate distance calculation~~e~~s that can compound when trying to quantify the object's dimensions. Therefore, while this method most closely aligns with the definition of measuring three mutually orthogonal axes, it is sensitive to data occlusions. In comparison to the RFCYLIN, the ~~RFCYCLIN~~ adjusted bounding box approach guarantees that the maximum dimensions will be measured. Therefore, this method is sensitive to outlier points, whereby ~~. Outlier points which deviate from the rockfall object, will be taken as~~ the maximum extents of complex geometry is defined using this approach. The RFSHAPZ approach attempts to bypass these complications by utilizing curve fitting approaches to assess the object dimensions ~~in light of~~ when there is non-uniform distribution of point density. This approach will not result in the maximum dimensions being selected, but rather representative dimensions based on the input point cloud. In comparison to the other methods, this method is the second most computationally demanding algorithm. The bounding box and adjusted bounding boxes are the least computationally demanding of the presented approaches. The adjusted bounding box is a robust approach that would work well in all environments when the input point clouds do not contain outlier points. ~~However~~When ~~, if~~ the input point clouds contain a uniform distribution of points, at the cost of some increased computational time, the RFCYLIN approach remains the closest to the definition of three mutually orthogonal axis based on the input point cloud.

Automated approaches have several advantages over manually classifying the dimensions of rockfall objects for a shape analysis. An automated approach removes the subjectivity that could potentially be induced by manually measuring an object. Increasing angularity or complex geometric features in the shapes can make it increasingly difficult to define orthogonal measurements for both manual and automated approaches. In comparison to manual measurements, however, an automated approach is repeatable because there is inherent subjectivity in the manual measurements depending ~~while depending~~ on the skill and experience of ~~who is conducting the manual measurement there is an inherent subjectivity~~person doing the work. In this work, the ~~authors have demonstrated that in the case of the~~ two independent sets of manual measurements for the White Canyon dataset differed depending on the complexity of the object~~there is subjectivity to how the dimensions are being measured~~. The classification resulting from the manual methods agreed in o~~O~~nly 34 ~~cases~~ of the 50 analysed cases. ~~had the same shape classification when the two datasets were compared.~~

In the interpretation of the results, i~~I~~t should be noted ~~, however,~~ that there are hard cut-offs between the different classes in the Sneed-Folk diagram. This can lead to circumstances where the object plots directly on ~~is treading~~ the line between two classes yet is assigned as single shape class. ~~However, this is a product of the Sneed and Folk classification which takes all the complexities of the 3D object and reduces it to a single class.~~

Almost all the automated fits attempt to find the maximum distance in order to define ~~ing~~ one of the ~~a~~ dimensions, except the RFSHAPZ approach. In comparison to the manual measurements, the measured dimension could be reflective of the overall dimension as opposed to the maximum. As illustrated with the case study of the synthetic objects, with increasing angularity and compactness, there is greater difficulty in defining the shortest axis of the objects. ~~Overall, u~~Underestimation of ~~ing~~ the shortest axis ~~of the objects,~~ will result in the objects being classified as flatter shapes, while ~~in comparison to~~ overestimation~~ng the shortest axis and the objects trending~~leads to classification in ~~towards~~ a more compact class.

Assessing the overall dataset of the 50 rockfall objects from the White Canyon, the shape classes trend toward “very-elongate” to “very-bladed”. ~~,~~ ~~this~~ This is the ~~a~~ direct result of the orientations of the joint sets and foliation within the rockmass which promotes the generation of these shapes. This result is in contrast to work previously done on this slope by van Veen et al. (2017), where the rockfall shapes were mostly ~~. In their study, they found a~~ cubic: this ~~trend which~~ is a direct result of the bounding box approach implemented in their study.

The differences in shape classification has direct implications for rockfall modelling. The size and shape of rock blocks are vital components when considering and assessing potential runout trajectories. Shape has been noted to affect the degree to which rolling can be sustained for blocks (Kobayashi et al., 1990). Furthermore, the degree of angularity of a block also has implications for transitions between translational and rotational motion (Pfeiffer and Bowen, 1989).

Industry standard rockfall modelling software packages such as RockyFor3D (Dorren, 2016) still use relatively simple geometric shapes (rectangles, ellipsoids, spheres). Therefore, if we consider the simulation of a cuboid or rectangular prism, where the volume can be defined as a product of the three axes; the measured dimensions directly influence~~s~~ the volume of the rockfall being simulated. The volume then defines the mass of the object and as a result, the moment of inertia.

~~TalThe shape or form of an object can be classified by assessing aspect ratios of major axes. However, it has been noted that a problem with this approach arises because there is no standardised method used to determine axis length or to assess if the axis measurements should be mutually orthogonal or not. Additionally, there is an inherent ambiguity in selecting the geometric axes of a particle (Blott and Pye, 2008) such that the A axis represents the maximum possible dimension and the B and C axes represent the intermediate and smallest dimensions respectively.~~

~~In this study, we have presented and compared six different methods for assessing a rockfall object’s dimensions and resulting shape. All of the algorithms have been presented which will permit these approaches to be replicated for future works. In~~

addition, we have created a synthetic dataset of rockfall objects that can be used to assess the effectiveness of new algorithms aimed at determining a rockfall object's dimensions. This represents a step forward in standardizing methodologies for best-practice in generating remotely sensed rockfall databases.

The results of this study confirm that the method used to measure the rockfall object's dimensions results in significantly different shape classifications. We have demonstrated that a bounding box approach can define a more cubic form of the object, if the orientation of the longest axis of the rockfall object is not parallel with one of the major Cartesian axes. If a bounding box will be used to determine the object's dimensions, the adjusted bounding box approach should be used instead.

A minimum bounding sphere was shown to be highly inappropriate for dimension extraction in the cases analyzed in this work. The approach results in all dimensions of the object being equal and every single object being classified as compact or equant (i.e. A=B=C). This may be valid for rockfall objects in some narrowly defined geological settings where equant blocks are released by the slope rockmass. In addition, further work is required to assess the applicability of the minimum bounding sphere approach to assess the dimensions of detached cobbles and boulders from select horizons of postglacial river terraces (Bonneau and Hutchinson, 2018a, 2018b).

The RFCYLIN approach introduced in the study is the most computationally demanding algorithm. The method tries to standardize an approach to measure dimensions, where each axis is measured orthogonally to one another, after the longest dimension has been defined. However, occlusions and edge effects in change detection analysis can result in inaccurate distance calculations which affect the object's dimensions. The RFSHAPZ approach attempts to bypass this complication by utilizing curve fitting methods to assess the dimensions even where there is non-uniform point density.

It should be noted that all the automated fits attempt to find the maximum distance defining a dimension. In comparison to the manual measurements, the measured dimension could be reflective of the overall dimension as opposed to the maximum. Increasing angularity or complex features in the shapes can make it increasingly difficult to define orthogonal measurements manually.

The differences in shape classification have direct implications for rockfall modelling. The size and shape of rock blocks affects potential runout trajectories substantially. Shape has been noted to affect the degree to which rolling can be sustained for blocks (Kobayashi et al., 1990). Furthermore, the degree of angularity of a block also has implications for transitions between translational and rotational motion (Pfeiffer and Bowen, 1989).

Industry standard rockfall modelling software packages such as RockyFor3D (Dorren, 2016) still use relatively simple geometric shapes (rectangles, ellipsoids, spheres). Therefore, if the simulation of a cuboid or rectangular prism is considered, where the volume can be defined as a product of the three axes; the measured dimension directly influences the volume of the rockfall being simulated. The volume then defines the mass of the object and as a result, the moment of inertia.

Fityus et al. (2013) found that the size and shape of rockfall debris are statistically different depending on the geological environment. In their study, they measured the three principal orthogonal dimensions of rock block debris with a measuring tape in a variety of geological settings to explore the effect of geology on the size and shape of rockfall debris. They outline that size distribution data used with shape distribution data could be used to undertake stochastic modelling of rockfalls to estimate the likely trajectories for a rockfall risk assessment. Therefore, depending on how the shape is measured, different shape classes may or may not be used in modelling. In our study, for the 50 rockfall events in the White Canyon, depending on which methodology was used to measure the object's dimensions, significantly different shape classifications were produced. If the bounding box approach is used, all shape classes are represented while all other fits including manual measurements trend towards the very-bladed to very-elongate shapes. Therefore, if forward modelling was to be undertaken, we might choose to exclude certain shapes depending on the methodology used to calculated rockfall dimensions.

5 Conclusions

In this study, we have demonstrated that the method used to measure the dimensions of rockfall objects matters. Depending on the method used, the object's shape may be misclassified into non-representative geometric categories. The classification of shape has implications for rockfall modelling used for the assessment of rockfall hazards when using shape classifications as input to rockfall modelling. Shape has been shown to have a large influence on runout distance. Therefore, it is imperative to select a robust method that can accurately and efficiently determine the dimensions of a rockfall object.

As illustrated with the analysis of synthetic blocks, increasing compactness and angularity results in the most difficulties in measuring the dimensions of a rockfall object. All automated methods and manual measurements displayed less scatter for the rounded dataset in comparison to their angular counterparts. Furthermore, there is a decrease in differences between the calculated dimensions as the object becomes less compact. This is best illustrated with the synthetic very-bladed and very-elongate blocks. The dimensions of both the angular and rounded version resulted in minimal scatter in the calculated dimensions. The differences between the lengths of the long, intermediate and short axes for these blocks are quite apparent. Therefore, both the manual and automated methods can converge on a dimension length and are not subject to the uncertainties created when there are similarities in the length of 2 or 3 of the axes.

The shape of real rockfall objects are quite complex, as displayed with the White Canyon dataset, where the results of the different axis measuring methods were quite variable. Angularity, non-uniform point spacing and occlusion in the rockfall object point clouds results in complications for extracting dimensions with both manual and automated methods. From the analysis of 50 rockfall events in the White Canyon, it appears that the RFSHAPZ method most closely aligns with the manual measurements. However, a comparison between the manual measurements shows that t~~T~~hese measurements ~~, however,~~ are ~~still~~ different. The manual method relies on the user consistently determining ~~Manually measuring the dimensions of an object can trend towards picking or measuring~~ a representative length, as opposed to automated methods which attempt to find the length of the maximum dimension~~s length~~. ~~Further to this, we have demonstrated that the methodology used to extract dimensions can vary significantly as demonstrated with the detailed rockfall case from the overall 50 events in the White Canyon.~~

The adjusted bounding box is the most robust approach presented in this study; however, the results can be sensitive to outlier points, leading to a potentially significant over estimation of the block volume, particularly for complex objects. The bounding box approach should not be used in any future studies. The two methods introduced in this study, ~~are the most computationally demanding of all the presented approaches. These two methods (~~RFCYLIN and RFSHAPZ, ~~)~~ were designed to standardize the way in which the dimensions are measured and work around challenges such as non-uniform point density and increasing angularity, while staying most closely aligned with the definition of measuring three mutually orthogonal axes. These two methods are however, the most computationally demanding of all the presented approaches.

Contributions

David A. Bonneau coordinated the study, generated all algorithms and code, and drafted the manuscript. David A. Bonneau and D. Jean Hutchinson co-analysed the data. Melanie Coombs and Paul-Mark Difrancesco ran code. Zac Sala generated the synthetic block dataset. All co-authors reviewed and edited the manuscript. All authors declare they have no conflict of interest.

Acknowledgements

This research was funded by the Natural Sciences and Engineering Research Council of Canada (NSERC) Discovery grant~~s held by D. Jean Hutchinson~~ and by the Canadian Railway Ground Hazards Research Program funding (CN Rail, CP Rail, Transport Canada, Geological Survey of Canada), held by D. Jean Hutchinson. Support was also provided to David A. Bonneau by the NSERC~~’s~~ Graduate Scholarship Program. Past and present Queen’s RGHRP team members are greatly acknowledged for their help with data collection.

References

Abellán, A., Oppikofer, T., Jaboyedoff, M., Rosser, N. J., Lim, M. and Lato, M. J.: Terrestrial laser scanning of rock slope instabilities, Earth Surf. Process. Landforms, 39(1), 80–97, doi:10.1002/esp.3493, 2014.

Abbott, B., Bruce, I., Savigny, W., Keegan, T., and Oboni, F.: A Methodology for the Assessment of Rockfall Hazard Risk along Linear Transportation Corridors, 8th International Association of Engineering Geology Conference, A Global View from the Pa- cific Rim, Vancouver, BC, 1998

Agisoft LLC: Agisoft PhotoScan User Manual, St. Petersburg, Russia. [online] Available from: www.agisoft.ru, 2018.

Benjamin, J.: Regional-scale controls on rockfall occurrence, PhD Thesis**,** Durham University., 2018.

Besl, P. and McKay, N.: A Method for Registration of 3-D Shapes, IEEE Trans. Pattern Anal. Mach. Intell., 14(2), 239–256, doi:10.1109/34.121791, 1992.

Blender: Blender - a 3D modelling and rendering package, [online] Available from: http://www.blender.org, 2018.

Bonneau, D. A. and Hutchinson, D. J.: Applications of Remote Sensing for Characterizing Debris Channel Processes, in Landslides: Putting Experience, Knowledge and Emerging Technologies into Practice., edited by J. V. De Graff and A. Shakoor, pp. 748–759, Association of Environmental & Engineering Geologists (AEG), Roanoke, USA., 2017.

Bonneau, D. A. and Hutchinson, D. J.: The Use of Multi-Scale Dimensionality Analysis for the Characterization of Debris Distribution Patterns, in Geohazards 7 - Engineering Resiliency in a Changing Climate, p. 8, Canmore, Alberta., 2018a.

Bonneau, D. A. and Hutchinson, D. J.: The use of terrestrial laser scanning for the characterization of a cliff-talus system in the Thompson River Valley, British Columbia, Canada, Geomorphology, doi:10.1016/j.geomorph.2018.11.022, 2018b.

Brown, D. A.: Geology of the Lytton Area, British Columbia, BSc Thesis, Carleton University., 1981.

Carrea, D., Abellan, A., Derron, M. H. and Jaboyedoff, M.: Automatic Rockfalls Volume Estimation Based on Terrestrial Laser Scanning Data, in Engineering Geology for Society and Territory - Volume 2: Landslide Processes, edited by G. Lollino, D. Giordan, G. B. Crosta, J. Corominas, R. Azzam, J. Wasowski, and N. Sciarra, pp. 1–2177, Springer International Publishing, Cham., 2015.

Cloutier, C., Locat, J., Geertsema, M., Jakob, M. and Schnorbus, M.: Potential impacts of climate change on landslides occurrence in Canada, edited by K. Ho, S. Lacasse, and L. Picarelli, Slope Saf. Prep. Impact Clim. Chang., (January 2017), 71–104, doi:10.1201/9781315387789-5, 2016.

Dorren, L. K. A.: Rockyfor3D (v5.2) Revealed – Transparent Description of the Complete 3D Rockfall Model, Geneva, Switzerland. [online] Available from: www.ecorisq.org, 2016.

Dussauge, C., Grasso, J.-R. and Helmstetter, A.: Statistical analysis of rockfall volume distributions: Implications for rockfall dynamics, J. Geophys. Res. Solid Earth, 108(B6), doi:10.1029/2001JB000650, 2003.

Ester, M., Kriegel, H.-P., Sander, J. and Xu, X.: A Density-Based Algorithm for Discovering Clusters in Large Spatial Databases with Noise, in Knowledge Discovery and Data Mining 1996, pp. 226–231, Elsevier., 1996.

Froude, M. J. and Petley, D. N.: Global fatal landslide occurrence from 2004 to 2016, Nat. Hazards Earth Syst. Sci., 18(8), 2161–2181, doi:10.5194/nhess-18-2161-2018, 2018.

Glover, J.: Rock-shape and its role in rockfall dynamics, PhD Thesis, 266, 2015.

Golub, G. H. and Loan, C. F. V: Matrix Computations, Book, 10(8), 48, doi:10.1063/1.3060478, 1996.

Guerin, A., Hantz, D., Rossetti, J.-P. and Jaboyedoff, M.: Brief communication"Estimating rockfall frequency in a mountain limestone cliff using terrestrial laser scanner", Nat. Hazards Earth Syst. Sci. Discuss., 2(1), 123–135, doi:10.5194/nhessd-2-123-2014, 2014.

Guzzetti, F., Reichenbach, P. and Ghigi, S.: Rockfall hazard and risk assessment along a transportation corridor in the Nera valley, central Italy, Environ. Manage., 34(2), 191–208, doi:10.1007/s00267-003-0021-6, 2004.

Hungr, O., Evans, S. G. and Hazzard, J.: Magnitude and frequency of rock falls and rock slides along the main transportation corridors of southwestern British Columbia, Can. Geotech. J., 36(2), 224–238, doi:10.1139/t98-106, 1999.

Hungr, O., Leroueil, S. and Picarelli, L.: The Varnes classification of landslide types, an update, Landslides, 11(2), 167–194, doi:10.1007/s10346-013-0436-y, 2014.

Jaboyedoff, M., Oppikofer, T., Abellán, A., Derron, M. H., Loye, A., Metzger, R. and Pedrazzini, A.: Use of LIDAR in landslide investigations: A review, Nat. Hazards, 61(1), 5–28, doi:10.1007/s11069-010-9634-2, 2012.

Janeras, M., Jara, J. A., Royán, M. J., Vilaplana, J. M., Aguasca, A., Fàbregas, X., Gili, J. A. and Buxó, P.: Multi-technique approach to rockfall monitoring in the Montserrat massif (Catalonia, NE Spain), Eng. Geol., 219, 4–20, doi:10.1016/j.enggeo.2016.12.010, 2017.

Jolivet, D., MacGowan, T., McFadden, R. and Steel, M.: Slope Hazard Assessment using Remote Sensing in White Canyon, Lytton, BC, Kingston, ON., 2015.

Kromer, R. A., Hutchinson, D. J., Lato, M. J., Gauthier, D. and Edwards, T.: Identifying rock slope failure precursors using LiDAR for transportation corridor hazard management, Eng. Geol., 195, 93–103, doi:10.1016/j.enggeo.2015.05.012, 2015a.

Lague, D., Brodu, N. and Leroux, J.: Accurate 3D comparison of complex topography with terrestrial laser scanner: Application to the Rangitikei canyon (N-Z), ISPRS J. Photogramm. Remote Sens., 82, 10–26, doi:10.1016/j.isprsjprs.2013.04.009, 2013.

Lato, M., Diederichs, M. S., Hutchinson, D. J. and Harrap, R.: Optimization of LiDAR scanning and processing for automated structural evaluation of discontinuities in rockmasses, Int. J. Rock Mech. Min. Sci., 46(1), 194–199, doi:10.1016/j.ijrmms.2008.04.007, 2009.

Lato, M. J., Diederichs, M. S., Hutchinson, D. J. and Harrap, R.: Evaluating roadside rockmasses for rockfall hazards using LiDAR data: Optimizing data collection and processing protocols, Nat. Hazards, 60(3), 831–864, doi:10.1007/s11069-011-9872-y, 2012.

Lato, M. J., Hutchinson, D. J., Gauthier, D., Edwards, T. and Ondercin, M.: Comparison of airborne laser scanning, terrestrial laser scanning, and terrestrial photogrammetry for mapping differential slope change in mountainous terrain, Can. Geotech. J., 52(2), 129–140, doi:10.1139/cgj-2014-0051, 2015.

Li, Q. and Griffiths, J. G.: Least squares ellipsoid specific fitting, in Geometric Modeling and Processing, 2004. Proceedings, pp. 335–340, IEEE., 2004.

M. C. Powers: A New Roundness Scale for Sedimentary Particles, SEPM J. Sediment. Res., Vol. 23(2), 117–119, doi:10.1306/D4269567-2B26-11D7-8648000102C1865D, 1953.

Malamud, B. D., Turcotte, D. L., Guzzetti, F. and Reichenbach, P.: Landslide inventories and their statistical properties, Earth Surf. Process. Landforms, 29(6), 687–711, doi:10.1002/esp.1064, 2004.

Mathworks: Matlab, [online] Available from: https://www.mathworks.com, 2018.

Monger, J. W. H.: Structural evolution of the southwestern Intermontane belt, Ashcroft and Hope map areas, British Columbia, in Current Research, Part A, Geological Survey of Canada, pp. 349–358, Ottawa, Ontario., 1985.

Optech: ILLRIS Summary Specification Sheet., 2014.

Pesci, A., Teza, G. and Bonali, E.: Terrestrial laser scanner resolution: Numerical simulations and experiments on spatial sampling optimization, Remote Sens., 3(1), 167–184, doi:10.3390/rs3010167, 2011.

Rosser, N., Lim, M., Petley, D., Dunning, S. and Allison, R.: Patterns of precursory rockfall prior to slope failure, J. Geophys. Res. Earth Surf., 112(4), doi:10.1029/2006JF000642, 2007.

Sala, Z.: Game-Engine Based Rockfall Modelling: Testing and Application of a New Rockfall Simulation Tool, MASc Thesis, Queen's University., 2018.

Santana, D., Corominas, J., Mavrouli, O. and Garcia-Sellés, D.: Magnitude-frequency relation for rockfall scars using a Terrestrial Laser Scanner, Eng. Geol., 144–145, 50–64, doi:10.1016/j.enggeo.2012.07.001, 2012.

Schneider, P. and Eberly, D.: Geometric Tools for Computer Graphics, Elsevier., 2003.

Smith, M. W., Carrivick, J. L. and Quincey, D. J.: Structure from motion photogrammetry in physical geography, Prog. Phys. Geogr., 40(2), 247–275, doi:10.1177/0309133315615805, 2016.

Sneed, E. D. and Folk, R. L.: Pebbles in the Lower Colorado River , Texas a Study in Particle Morphogenesis, J. Geol., 66(2), 114–150, 1958.

Sturzenegger, M., Stead, D. and Elmo, D.: Terrestrial remote sensing-based estimation of mean trace length, trace intensity and block size/shape, Eng. Geol., 119(3–4), 96–111, doi:10.1016/j.enggeo.2011.02.005, 2011.

Telling, J., Lyda, A., Hartzell, P. and Glennie, C.: Review of Earth science research using terrestrial laser scanning, Earth-Science Rev., 169(March), 35–68, doi:10.1016/j.earscirev.2017.04.007, 2017.

Teza, G., Atzeni, C., Balzani, M., Galgaro, A., Galvani, G., Genevois, R., Luzi, G., Mecatti, D., Noferini, L., Pieraccini, M., Silvano, S., Uccelli, F. and Zaltron, N.: Ground-based monitoring of high-risk landslides through joint use of laser scanner and interferometric radar, Int. J. Remote Sens., 29(16), 4735–4756, doi:10.1080/01431160801942227, 2008.

Tonini, M. and Abellan, A.: Rockfall detection from terrestrial LiDAR point clouds: A clustering approach using R, J. Spat. Inf. Sci., 8(8), 95–110, doi:10.5311/JOSIS.2014.8.123, 2014.

van Veen, M., Hutchinson, D. J., Kromer, R., Lato, M. and Edwards, T.: Effects of sampling interval on the frequency - magnitude relationship of rockfalls detected from terrestrial laser scanning using semi-automated methods, Landslides, (January), 1–14, doi:10.1007/s10346-017-0801-3, 2017.

Volkwein, A., Schellenberg, K., Labiouse, V., Agliardi, F., Berger, F., Bourrier, F., Dorren, L. K. A., Gerber, W. and Jaboyedoff, M.: Rockfall characterisation and structural protection - A review, Nat. Hazards Earth Syst. Sci., 11(9), 2617–2651, doi:10.5194/nhess-11-2617-2011, 2011.

Welzl, E.: Smallest enclosing disks (balls and ellipsoids), in New Results and New Trends in Computer Science, vol. 555, edited by H. Maurer, pp. 359–370, Springer-Verlag, Berlin/Heidelberg., 1991.

Westoby, M. J., Brasington, J., Glasser, N. F., Hambrey, M. J. and Reynolds, J. M.: "Structure-from-Motion" photogrammetry: A low-cost, effective tool for geoscience applications, Geomorphology, 179, 300–314, doi:10.1016/j.geomorph.2012.08.021, 2012.

Wieczorek, G. F. and Jäger, S.: Triggering mechanisms and depositional rates of postglacial slope-movement processes in the Yosemite Valley, California, Geomorphology, 15(1), 17–31, doi:10.1016/0169-555X(95)00112-I, 1996.

Williams: Insights into Rockfall from Constant 4D Monitoring., 2017.

Williams, J. G., Rosser, N. J., Hardy, R. J., Brain, M. J. and Afana, A. A.: Optimising 4-D surface change detection: an approach for capturing rockfall magnitude–frequency, Earth Surf. Dyn., 6(1), 101–119, doi:10.5194/esurf-6-101-2018, 2018.

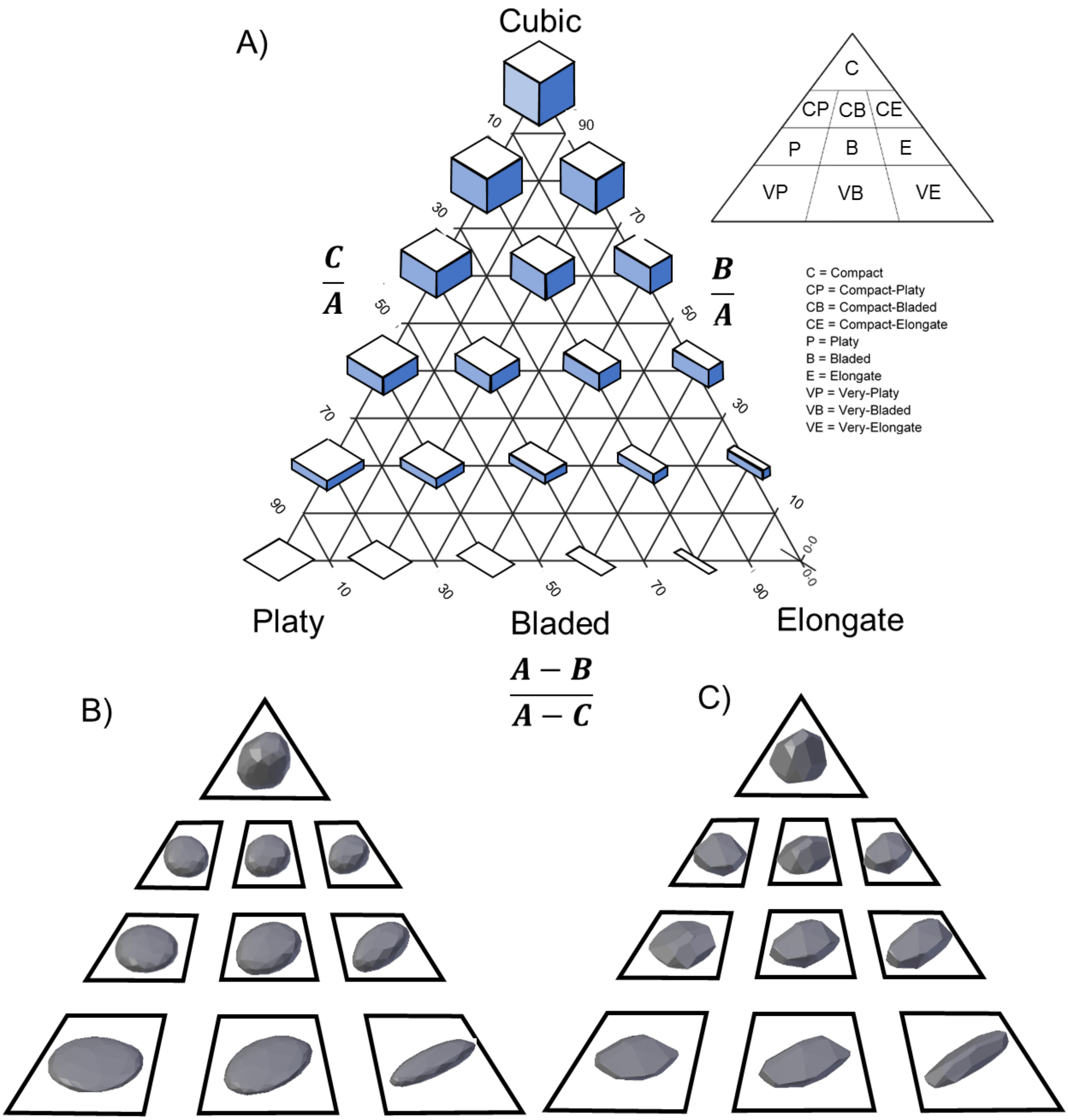

Figure 1. Overview of the Sneed and Folk ternary diagram adapted from Blott and Pye (2008). A) Visual representation of the different shape forms as defined by Sneed and Folk (1958). Inset diagrams display the divisions for each shape class. B) Overview of the rounded synthetic blocks generated using Blender. C) Overview of the angular blocks generated for the study.

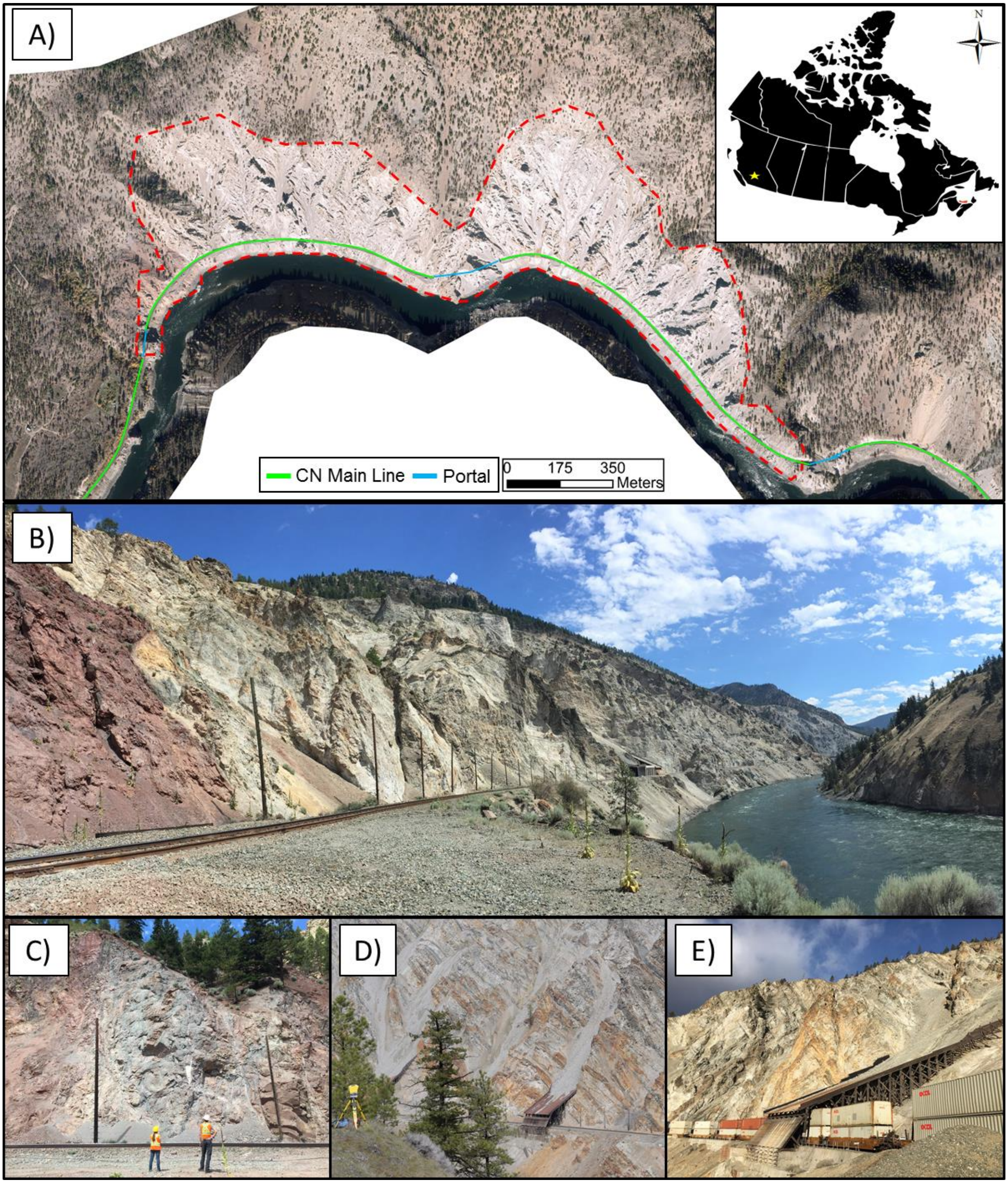

Figure 2. Location map of the White Canyon. A) October 2015 orthophoto of the White Canyon. The White Canyon is delineated by the red dashed line. B) July 2016 panoramic photograph from track level looking northeast at the complex morphology of the study slope. C) July 2016 photograph from track level of the Mt. Lytton Batholith. D) April 2017 photograph displaying the TLS system setup looking at the study slope from across the Thompson River. E) February 2018 photograph from track level looking at one of the rocksheds on the eastern portion of the canyon. The rockshed is 20 m in width.

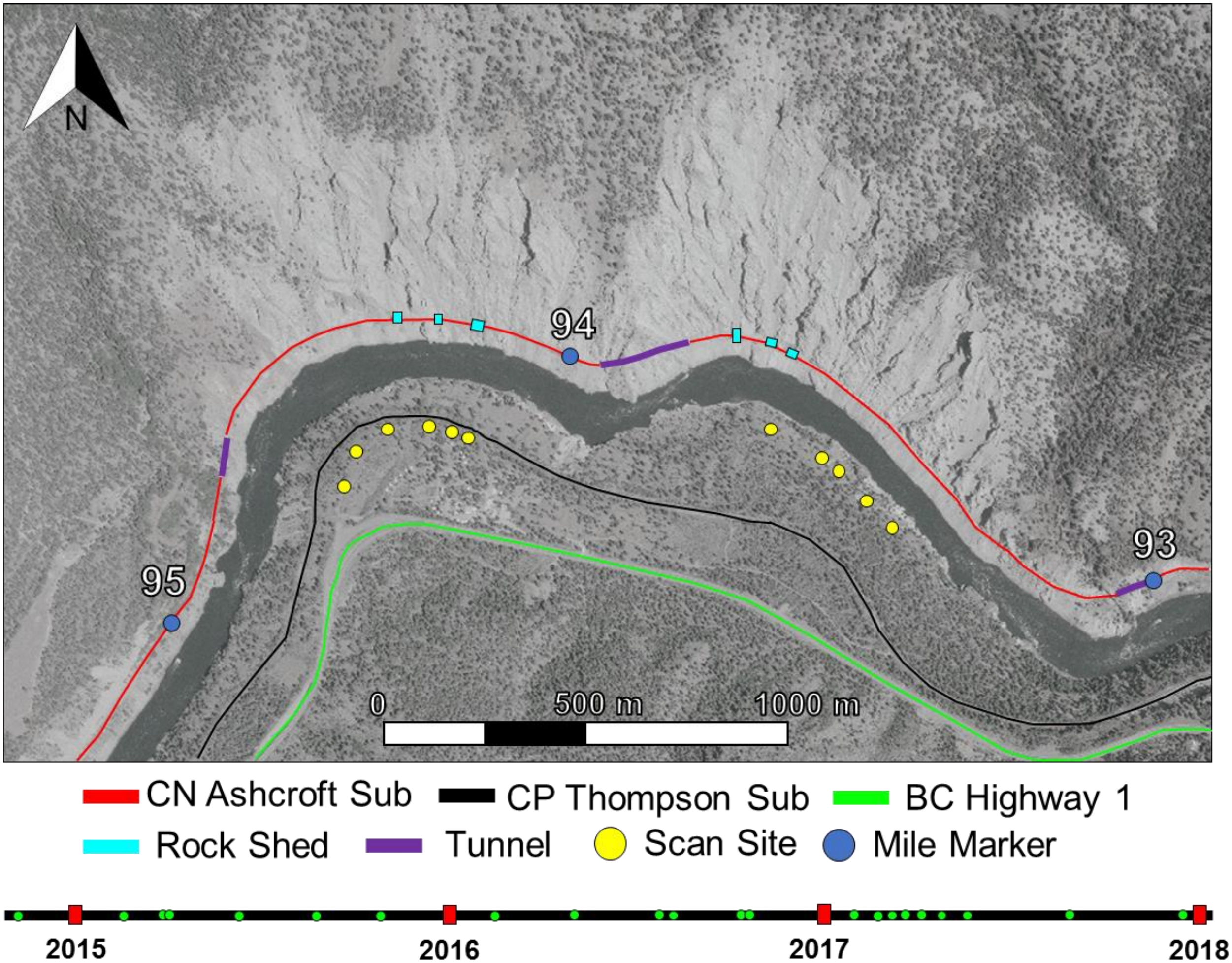

Figure 3. Overview of the scan site locations from across the Thompson River. The timeline across the bottom of the figure indicates the times when TLS scans were captured (green dots).

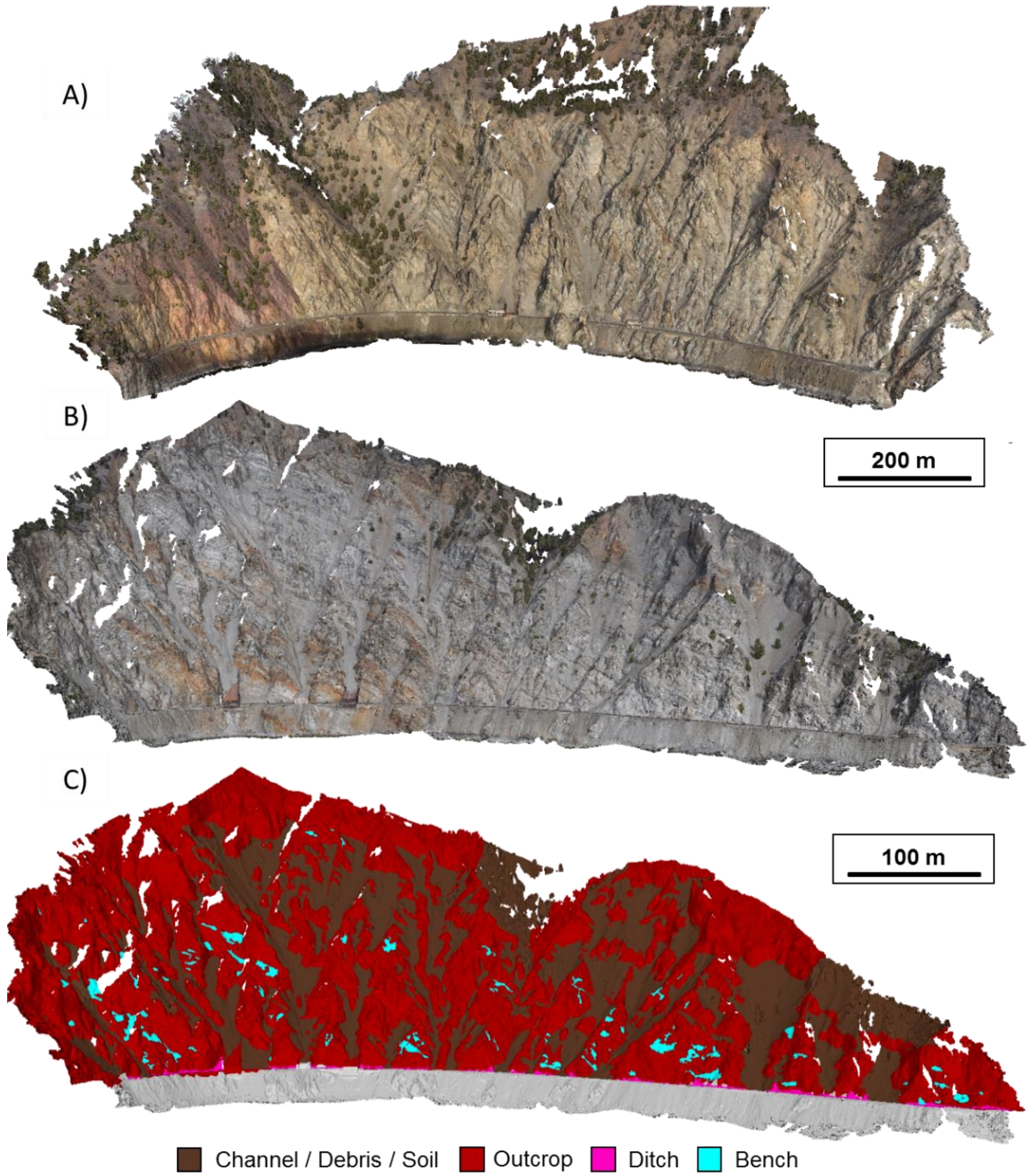

Figure 4. Overview of the SfM-MVS photogrammetry models. A) Model of WCW taken on January 30th, 2017. B) Model of WCE taken on April 4th, 2017. C) Classified model of WCE. The model was remotely mapped in PhotoScan using a combination of the RGB point cloud and visual inspection of the panoramic photography.

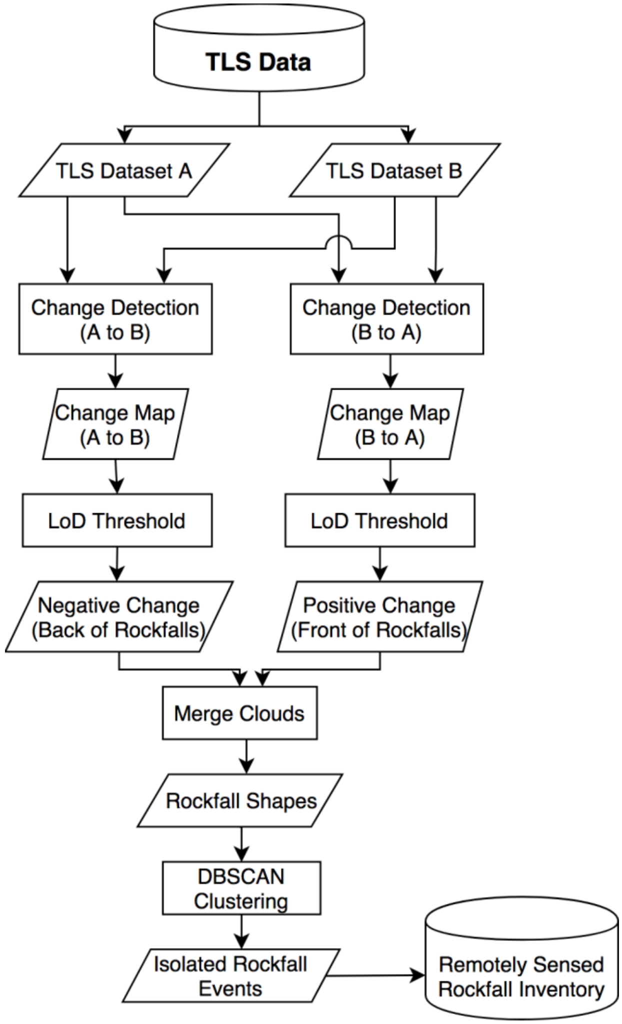

Figure 5. Structured flow chart of the semi-automated process of extracting rockfall from sequential TLS scans.

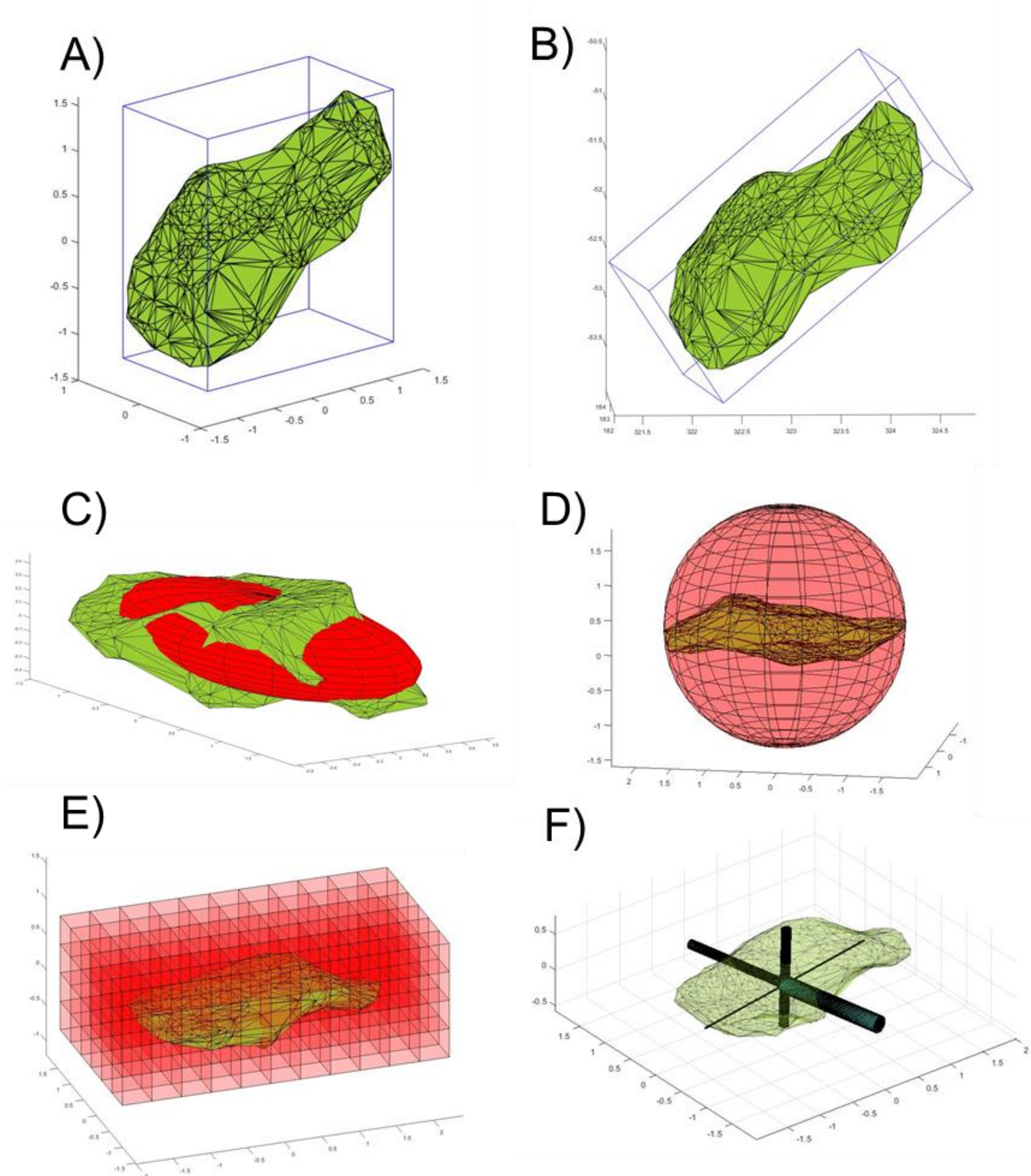

Figure 6. Visual representation of each of the model fitting methods used in the study. A) Bounding box approach (e.g. van Veen et al., (2017); Benjamin (2018); Williams (2017). B) Adjusted bounding box approach. C) Least-squares ellipsoid fit. D) Minimum bounding sphere fit. E) RFSHAPZ approach. F) RFCYLIN approach.

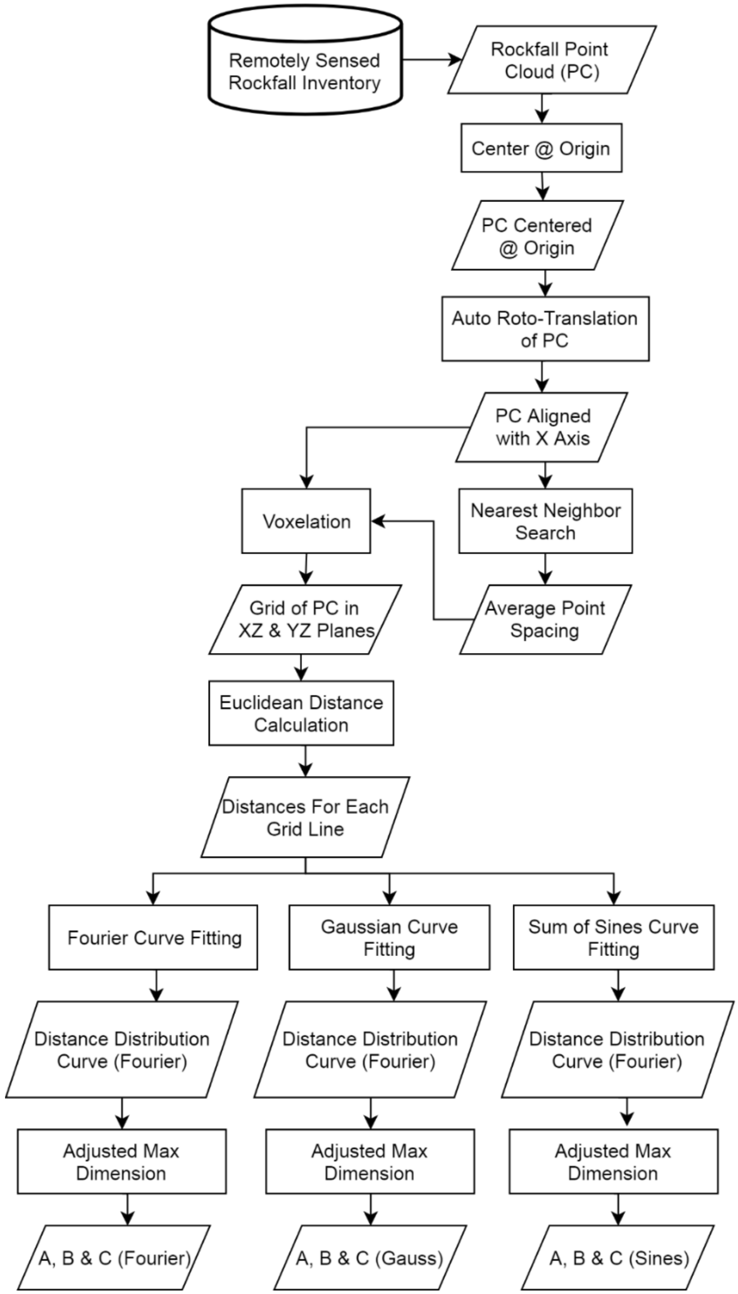

Figure 7. Structured flow chart of the RFSHAPZ algorithm.

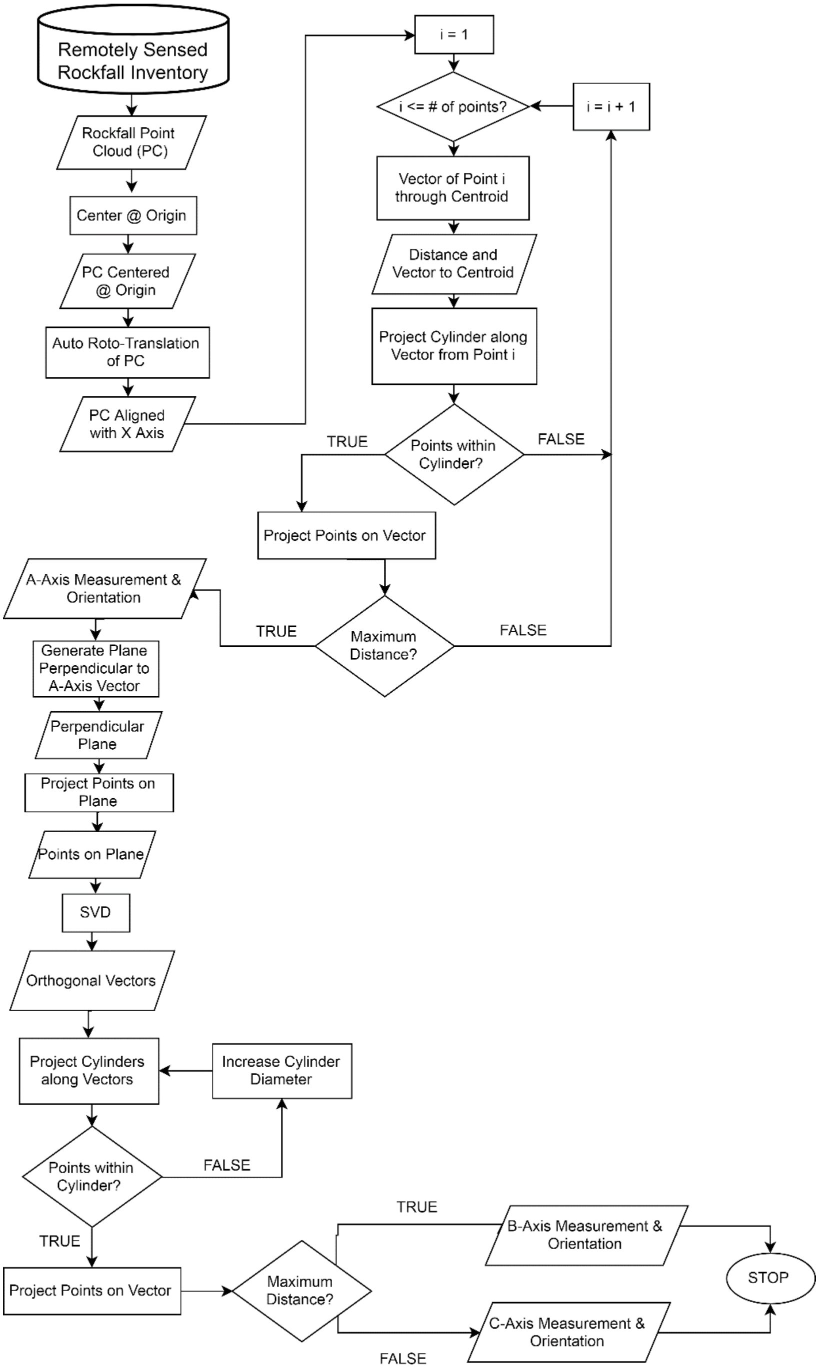

Figure 8. Structured flow chart of the RFCYLIN algorithm.

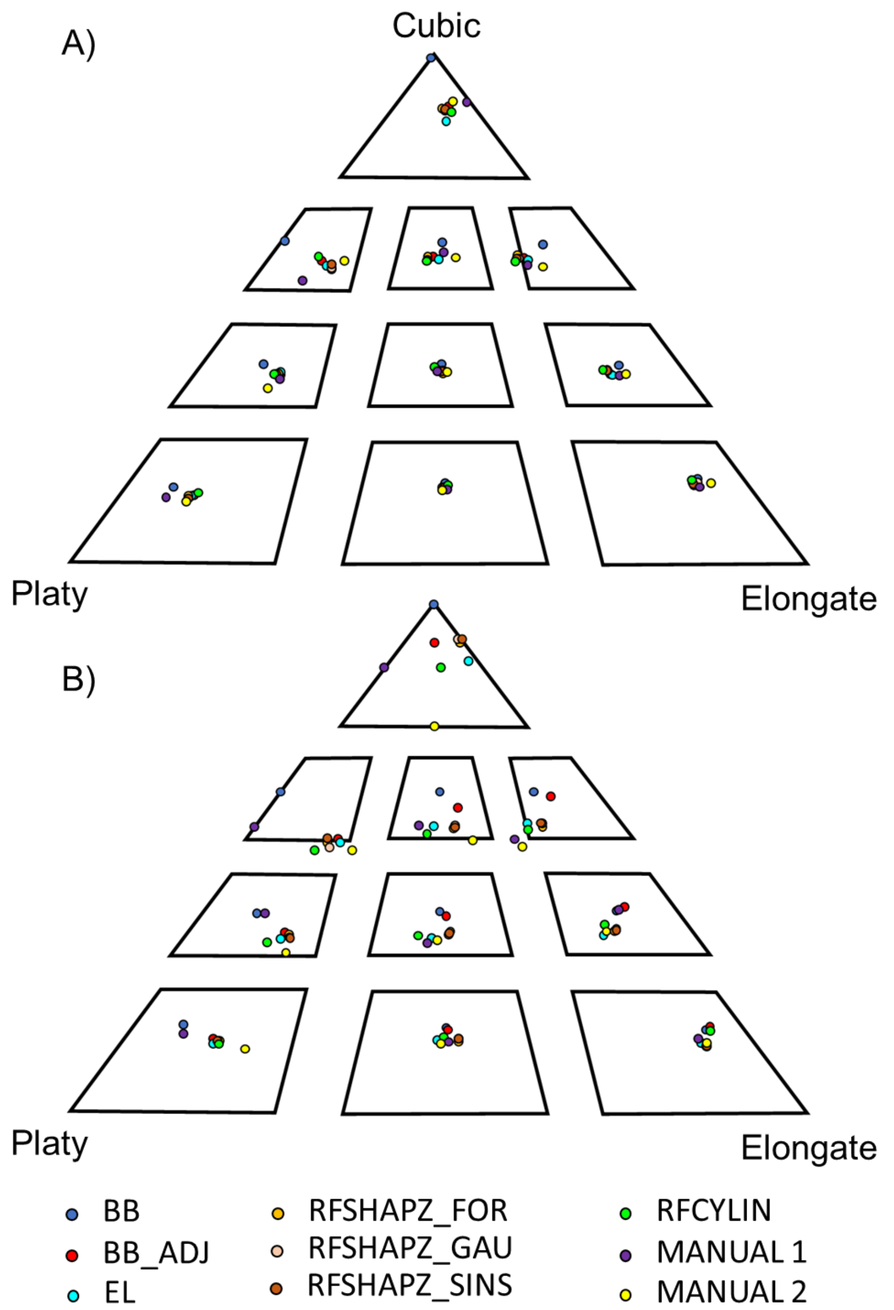
A)
Cubic
Platy
Elongate
B)
Platy
Elongate
BB
BB_ADJ
EL
RFSHAPZ_FOR
RFSHAPZ_GAU
RFSHAPZ_SINS
RFCYLIN
MANUAL 1
MANUAL 2

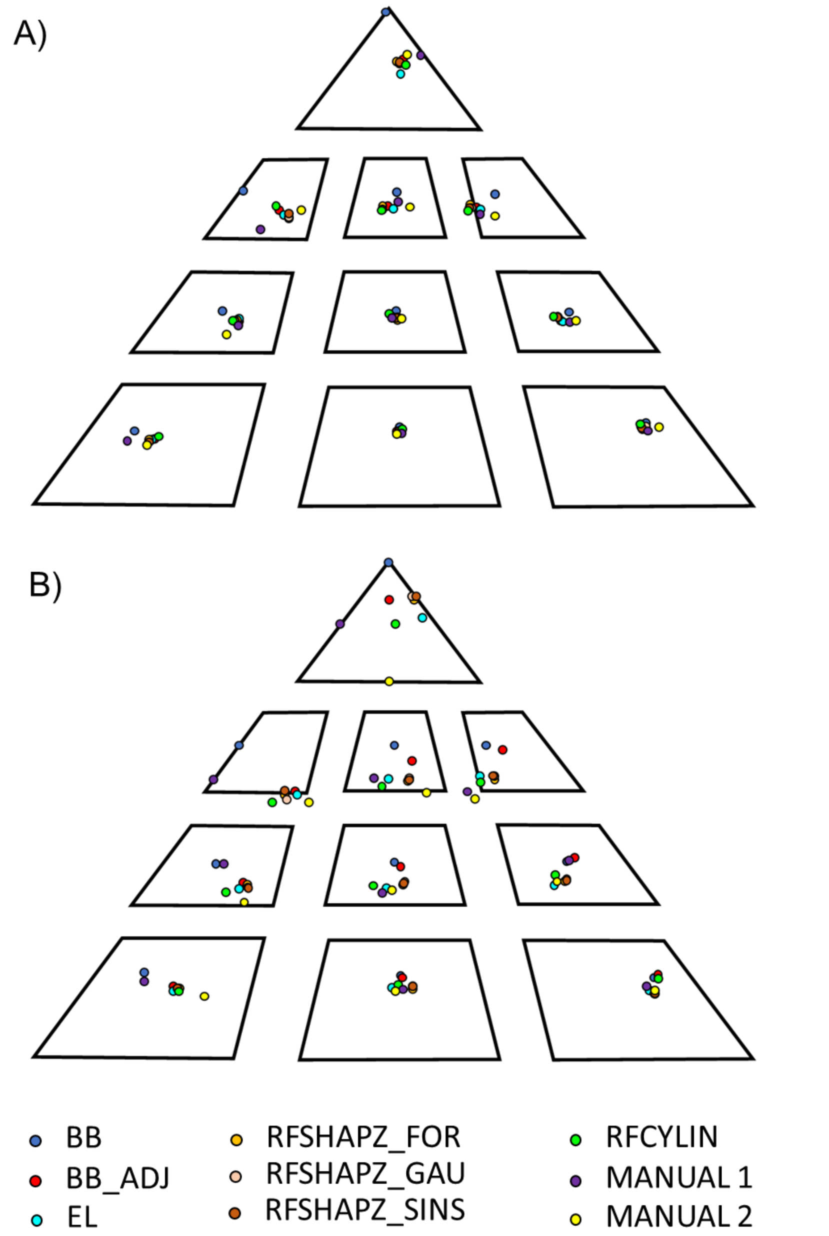

Figure 9. Sneed and Folk ternary diagrams separated to highlight shape classification results. A) Displaying the results of each of the 9 fits for each of the rounded synthetic blocks. B) Displaying the results of each of the fits for the angular synthetic blocks. BB: bounding box; BB_ADJ: adjusted bounding box; EL: Least-squares ellipsoidal fit; RFSHAPZ_FOR: RFSHAPZ Fourier fit; RFSHAPZ_GAU: RFSHPZ Gaussian fit; RFSHAPZ_SINS: RFSHAPZ Sum of Sines fit; RFCYLIN: RFCYLIN fit.

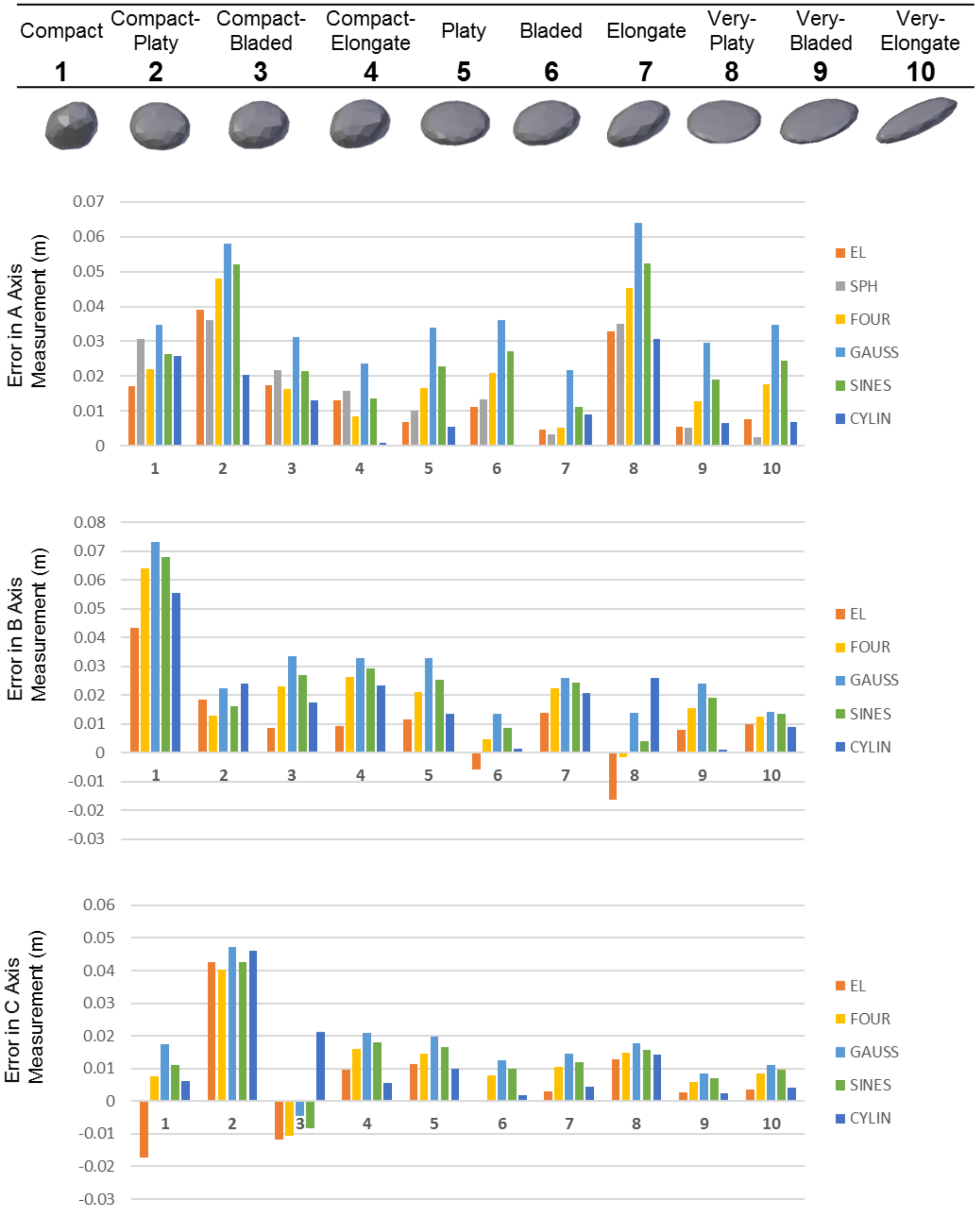

Figure 10. Error in dimension measurement for each fit compared to a set of manual measurements for the rounded synthetic blocks. **EL: Least-squares ellipsoidal fit; FOUR: RFSHAPZ Fourier fit; GAUSS: RFSHPZ Gaussian fit; SINES: RFSHAPZ Sum of Sines fit; CYLIN: RFCYLIN fit.**

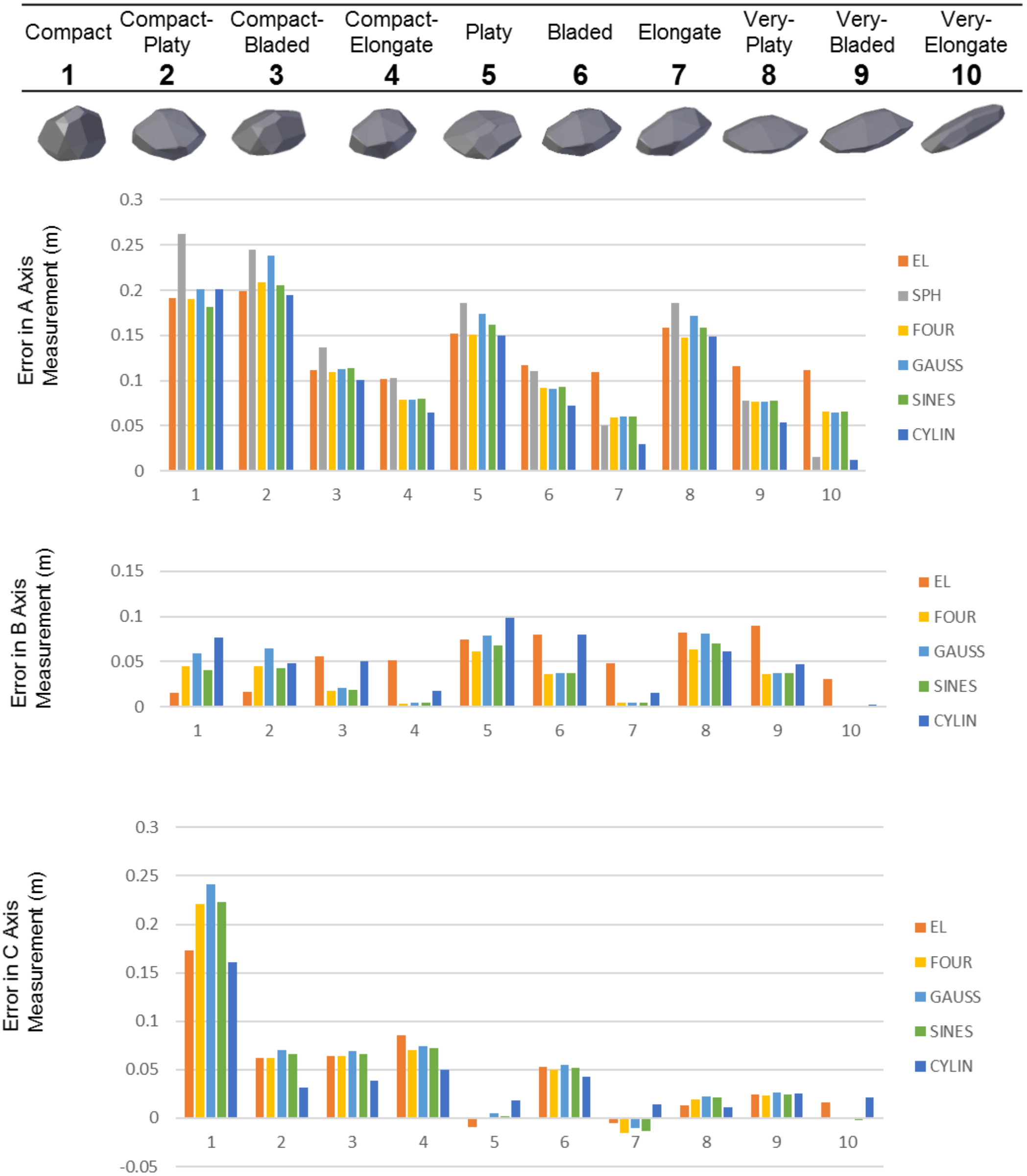

Figure 11. Error in dimension measurement for each fit compared to a set of manual measurements for the angular synthetic blocks. **SPH: minimum-bounding sphere fit; EL: Least-squares ellipsoidal fit; FOUR: RFSHAPZ Fourier fit; GAUSS: RFSHPZ Gaussian fit; SINES: RFSHAPZ Sum of Sines fit; CYLIN: RFCYLIN fit.**

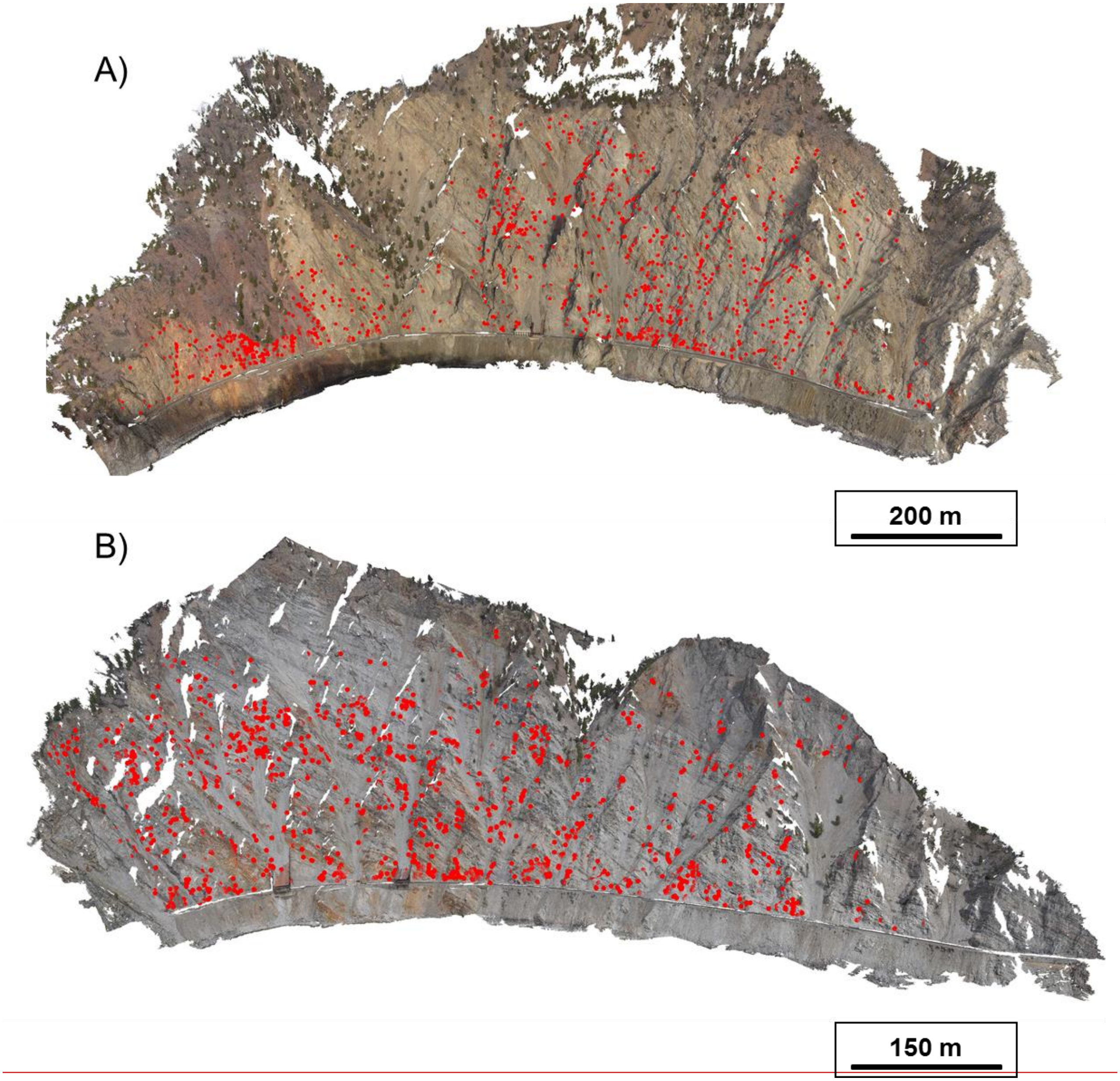
A)
200 m
B)
150 m

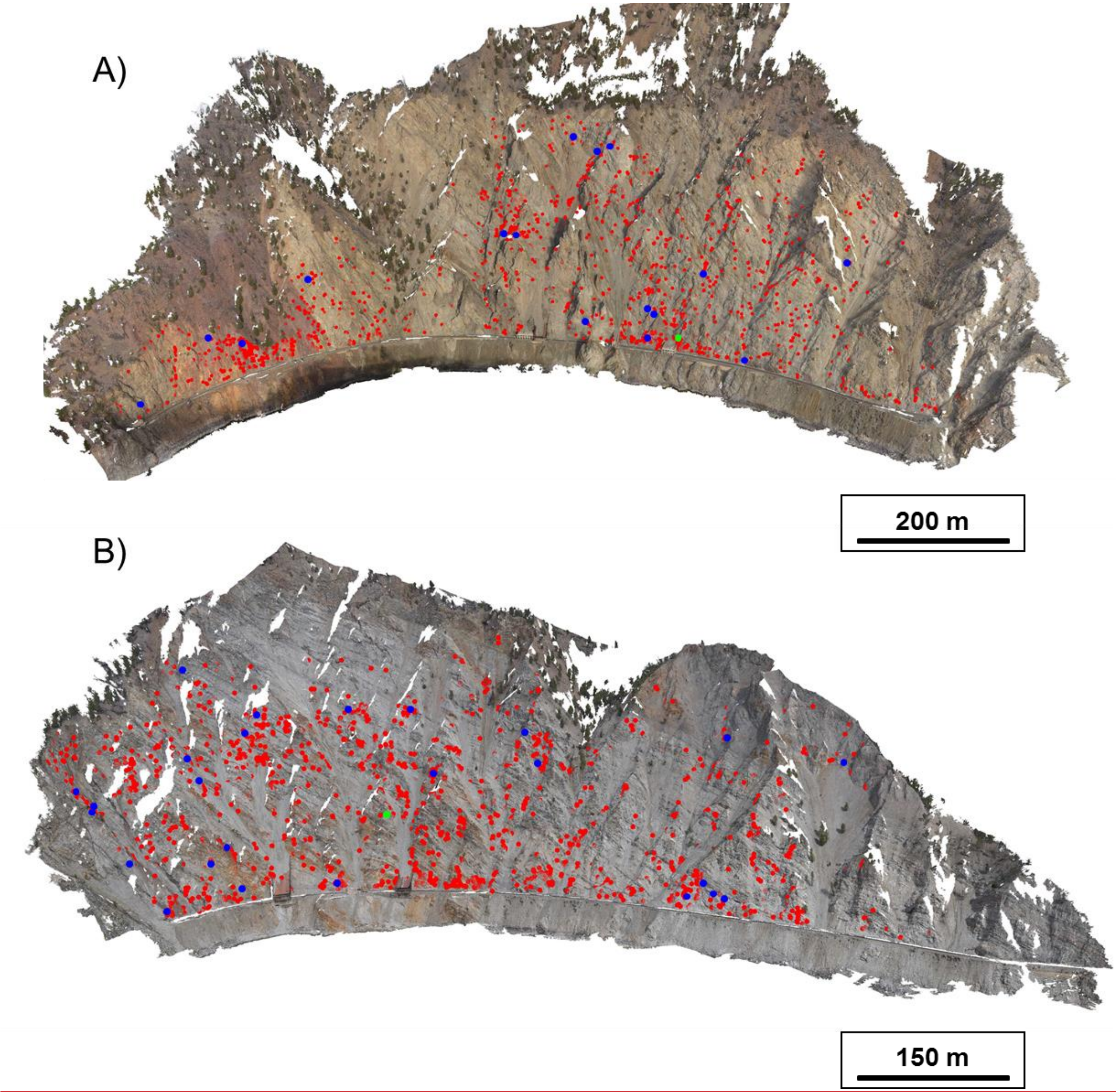

Figure 12. The White Canyon rockfall database. **The centroid of each rockfall event is displayed as a red dot on the photogrammetry model.** **The blue dots correspond to the 50 rockfall events analyzed in detail. The light green dots correspond to the events analyzed in Figure 14.** **A) White Canyon West results.** ~~**The centroid of each rockfall event is displayed as a red dot on the photogrammetry model.**~~ **B) White Canyon East results.**

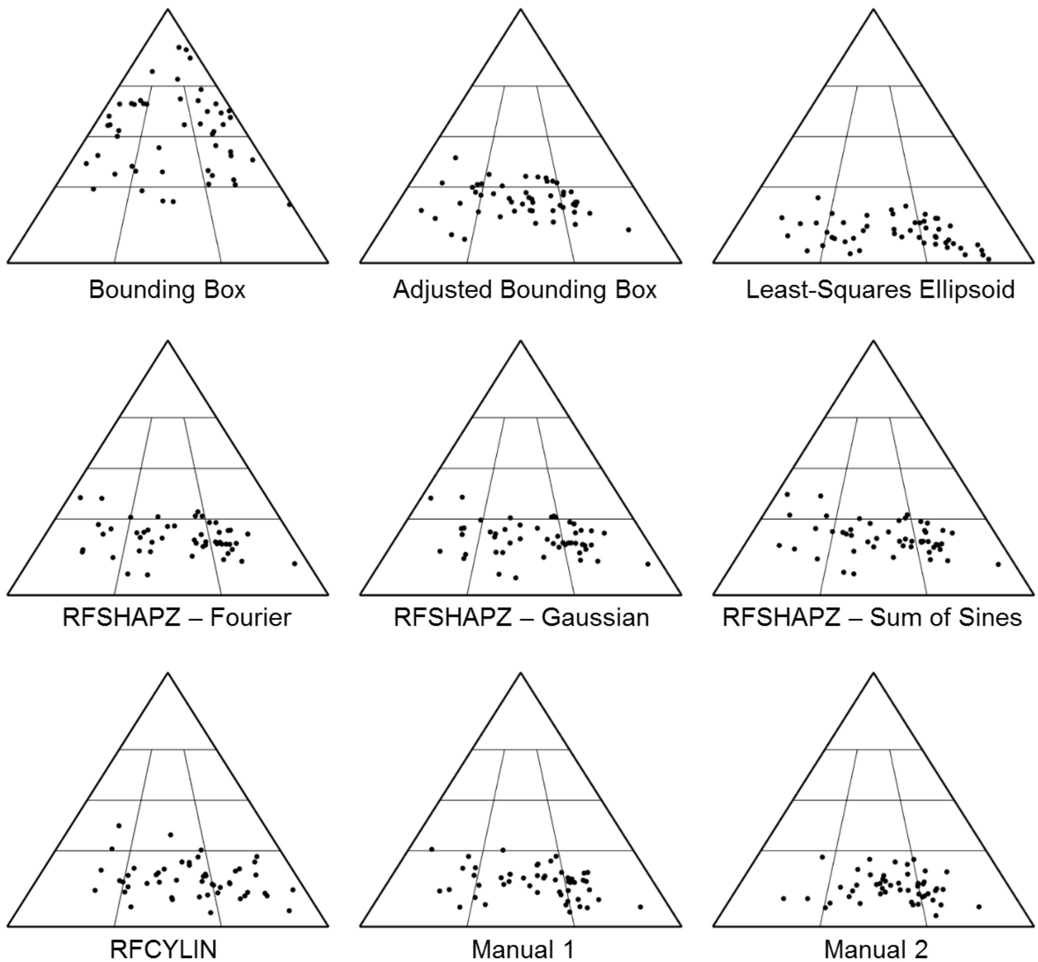
Bounding Box
Adjusted Bounding Box
Least-Squares Ellipsoid
RFSHAPZ – Fourier
RFSHAPZ – Gaussian
RFSHAPZ – Sum of Sines
RFCYLIN
Manual 1
Manual 2

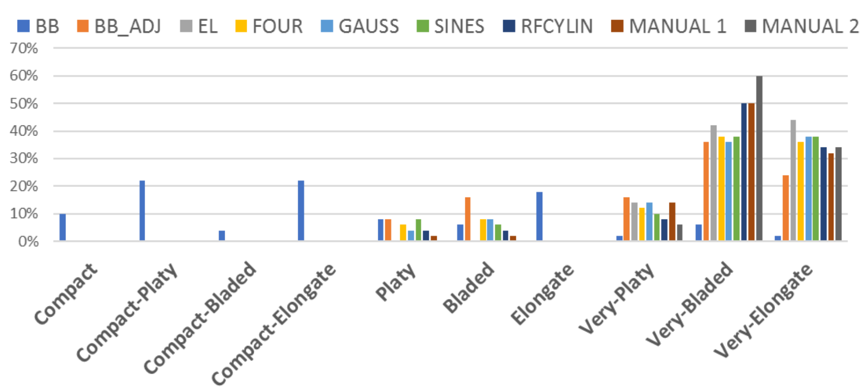
BB
BB_ADJ
EL
FOUR
GAUSS
SINES
RFCYLIN
MANUAL 1
MANUAL 2
70%
60%
50%
40%
30%
20%
10%
0%
Compact
Compact-Platy
Compact-Bladed
Compact-Elongate
Platy
Bladed
Elongate
Very-Platy
Very-Bladed
Very-Elongate

Figure 13. Sneed and Folk ternary diagrams for each of the model fits for the 50 rockfall events that occurred in the White Canyon. Bar chart at the bottom highlights the percentage of classes for each of the fits. BB: bounding box; BB_ADJ: adjusted bounding box; EL: Least-squares ellipsoidal fit; FOUR: RFSHAPZ Fourier fit; GAUSS: RFSHPZ Gaussian fit; SINES: RFSHAPZ Sum of Sines fit; RFCYLIN: RFCYLIN fit.

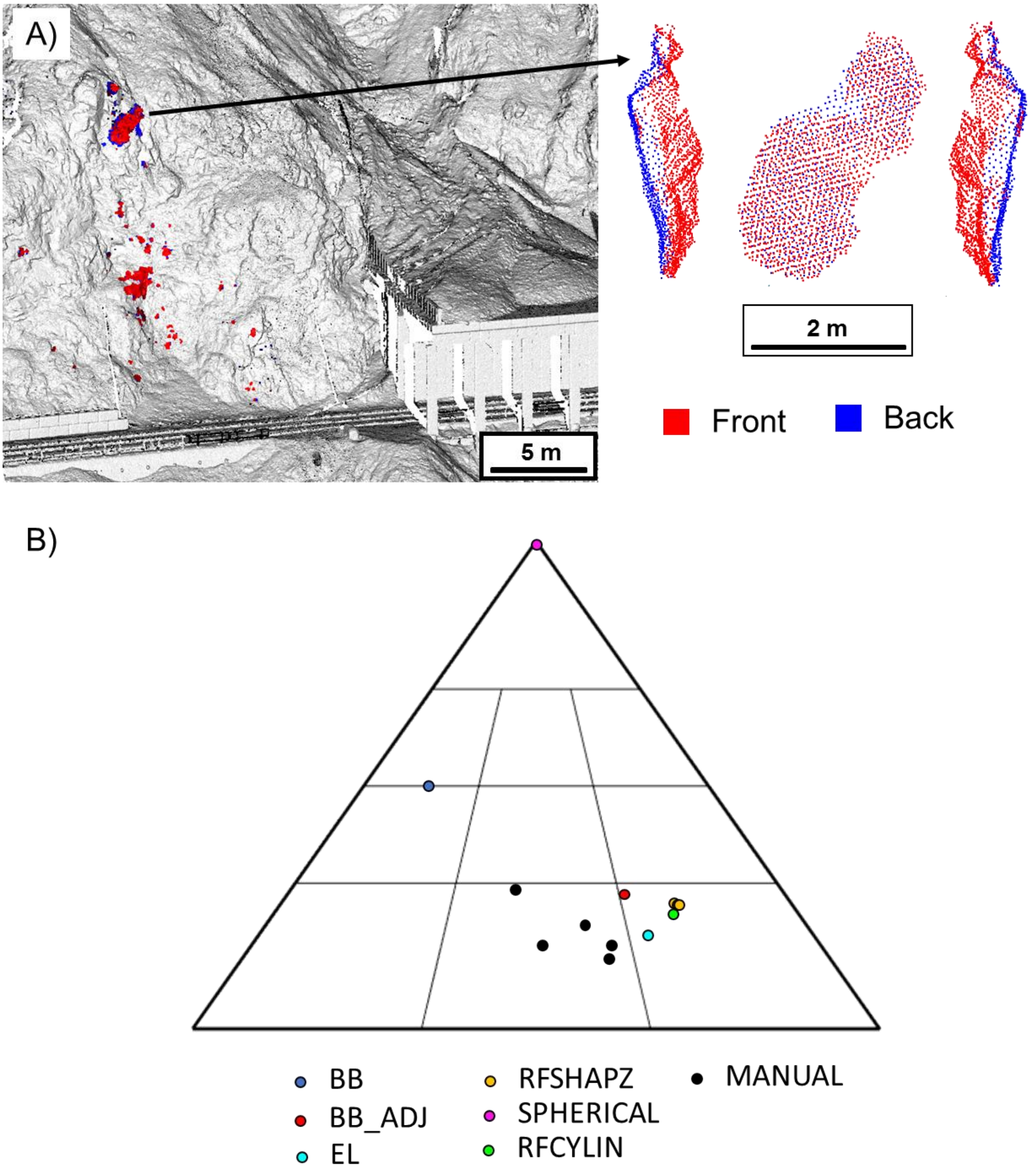

A)
5 m
2 m
Front
Back
B)
BB
BB_ADJ
EL
RFSHAPZ
SPHERICAL
RFCYLIN
MANUAL

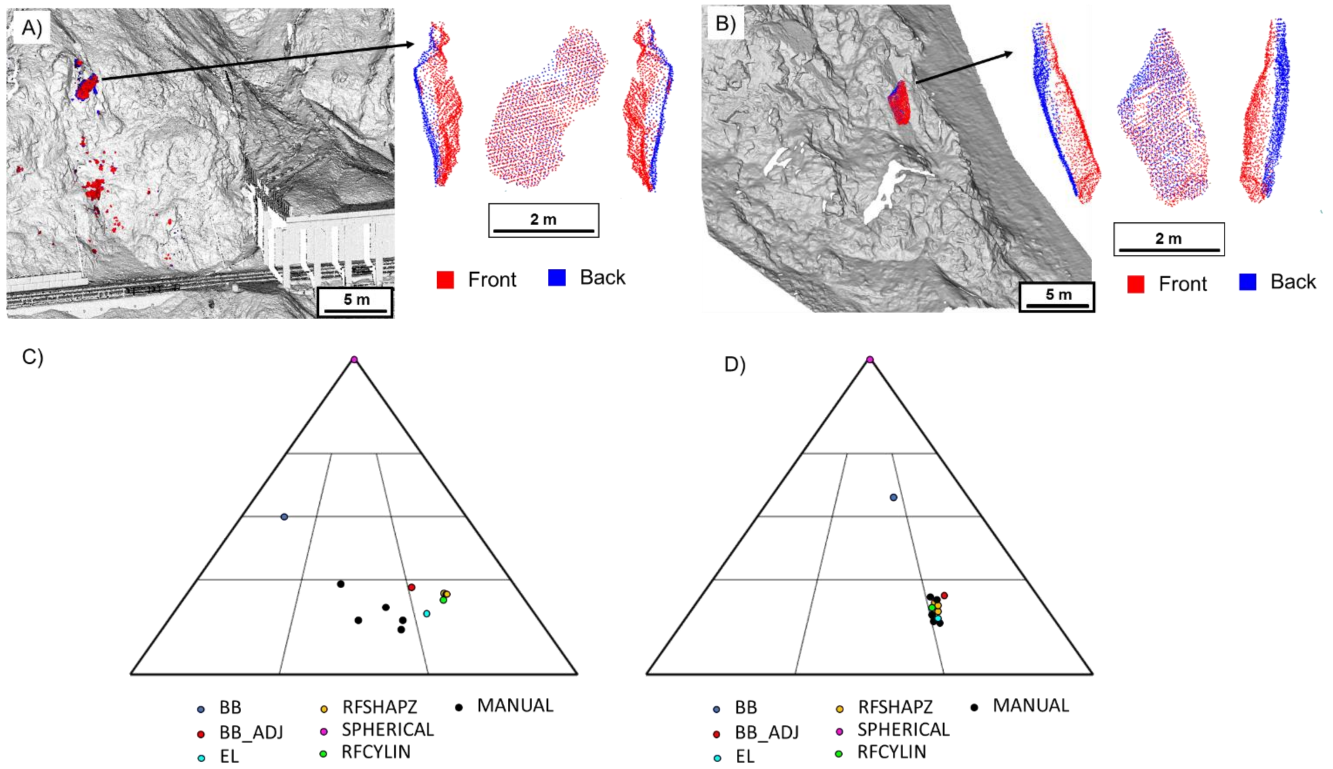

Figure 14. Overview of the two~~single~~ rockfall events analyzed in more detail, with manual measurements made by five different people. A) Displaying the spatial location and shape of the rockfall event in White Canyon West. ~~The shape of the rockfall object is also displayed.~~ The red points correspond to the front of the object while the blue points correspond to the back of the object. B) Displaying the spatial location and shape of the rockfall event in White Canyon East~~. The shape of the rockfall object is also displayed.~~ The red points correspond to the front of the object while the blue points correspond to the back of the object.~~the results of the fits for the rockfall object.~~ C) Displaying the results of the different fitting methods for the rockfall event shown in (A). D) Displaying the results of the different fitting methods for the rockfall event shown in (B). BB: bounding box; BB_ADJ: adjusted bounding box; EL: Least-squares ellipsoidal fit.